Applied Radiation and Isotopes 236 (2026) 112765

Contents lists available at ScienceDirect

Applied Radiation and Isotopes

journal homepage: www.elsevier.com/locate/apradiso

Thermoluminescence and anomalous heating-rate behavior in $SmBa_3B_9O_{18}$: Evidence for hierarchical trap distribution and strong retrapping dynamics

Jabir Hakami [a], O. Madkhali [a], M. Oglakci [b], E.A. Cin [c], E. Ekdal Karali [d], H. Orucu [e], M.B. Coban [f,g], U.H. Kaynar [h], N. Can [a,*]

[a] Jazan University, College of Science, Department of Physical Sciences, Physics Division, P.O. Box 114, Jazan, 45142, Kingdom of Saudi Arabia
[b] Physics Department, Cukurova University, Arts-Sciences Faculty, Adana, 01330, Türkiye
[c] Bakırcay University, Graduate School of Natural and Applied Sciences, Menemen, Izmir, Türkiye
[d] Ege University, Institute of Nuclear Sciences, Bornova, Izmir, 35100, Turkey
[e] Ege University, Science Faculty, Department of Physics, Izmir, 35040, Türkiye
[f] Balikesir University, Faculty of Arts and Sciences, Department of Physics, Balikesir, Türkiye
[g] Balikesir University, Science and Technology Application and Research Center, Balikesir, Türkiye
[h] Bakircay University, Faculty of Engineering and Architecture, Department of Fundamental Sciences, Menemen, Izmir, Türkiye

ARTICLE INFO

Keywords:
$SmBa_3B_9O_{18}$
Anomalous heating-rate behaviour
Trap hierarchy
T_m–T_{stop} analysis

ABSTRACT

$SmBa_3B_9O_{18}$ nanostructures were synthesized by a sol–gel assisted microwave combustion route and subsequently calcined at 800 °C, yielding a crystalline rare-earth-based borate host lattice for detailed thermoluminescence (TL) characterization. X-ray diffraction and Rietveld refinement confirm the formation of a single-phase structure with high crystallinity and well-defined lattice parameters. TL measurements recorded in a 565 nm band-pass detection window reveal well-resolved multi-peak glow curves suitable for detailed kinetic analysis. Preheating at 150 °C for 8 s effectively removes shallow traps and stabilizes the dosimetric signal, yielding dominant glow peaks at ~220 °C and ~290 °C associated with thermally stable trapping centers. The material shows a nearly linear dose response up to ~60 Gy, followed by controlled supralinearity up to 500 Gy, together with a low minimum detectable dose (~0.13 Gy) and excellent reusability, with cycle-to-cycle deviations within ±5%. Variable heating-rate experiments (0.2–4 °C s^{-1}) reveal pronounced anomalous heating-rate behavior, where both peak intensity and integrated TL signal increase with heating rate, deviating from conventional kinetic models. Combined various-heating-rate, T_m–T_{stop} and initial-rise analyses (with thermal-lag correction) yield activation energies of ~1.6–1.7 eV and ~1.9–2.0 eV for the main peaks and reveal characteristic plateau–shift behavior consistent with a hierarchical trap system comprising multiple overlapping and partially distributed trapping levels. Fading analysis shows non-monotonic behavior, with an initial TL increase of up to ~20% around 12 h followed by gradual decay, attributed to post-irradiation charge redistribution and thermally assisted retrapping within a coupled trap system. These results demonstrate that $SmBa_3B_9O_{18}$ is a promising TL dosimetric material, combining high structural stability, sensitive and reusable response, and complex non-classical luminescence kinetics governed by coupled trap–recombination dynamics.

1. Introduction

Borate-based phosphors have attracted sustained attention in radiation dosimetry and luminescent technologies owing to their good thermal and chemical stability, relatively low effective atomic number, and ease of synthesis in a wide variety of compositions and structures (Joseph et al., 2023; Kumar et al., 2019; Nabadwip Singh, 2021; Portakal Uçar, 2021). In borate hosts, intrinsic defects such as vacancies and defect complexes act as trapping and recombination centers, governing TL behavior under ionizing or UV irradiation (Linderälv et al., 2021; Stagi et al., 2024). Both undoped borate materials, where TL is purely intrinsic, and rare-earth-containing systems, where 4f ions strongly modify the defect landscape, have been explored for dosimetric and photonic applications (Alathlawi et al., 2025; Anishia et al., 2011; Kaynar et al., 2023; Ngoc et al., 2024; Oglakci et al., 2025).

In a TL process, irradiation creates electron–hole pairs that become

* Corresponding author.
E-mail address: ncan@jazanu.edu.sa (N. Can).

https://doi.org/10.1016/j.apradiso.2026.112765
Received 2 May 2026; Received in revised form 10 June 2026; Accepted 18 June 2026
Available online 23 June 2026

localized at trapping centers and recombination sites distributed within the bandgap. Upon controlled heating, thermally stimulated release of charge carriers leads to radiative recombination and the appearance of TL glow peaks whose shapes and positions are governed by trap depth, frequency factor, and kinetic order (Altowyan et al., 2024; Bulcar et al., 2021; Nabadwip Singh, 2021). Advanced kinetic methods (e.g., VHR, T_m–T_{stop}, and initial rise) reveal overlapping or quasi-continuous trap distributions in borate systems, reflecting complex defect environments and multiple recombination pathways (Altowyan et al., 2024; Bulcar et al., 2026; Guler and Gasanly, 2018). These methods are particularly essential for resolving non-ideal TL behavior arising from overlapping traps and retrapping processes. Intrinsic defects in borate networks, such as borate radicals and oxygen vacancies, influence carrier dynamics and trap stability. Charge-compensating defects associated with rare-earth ions may also affect recombination probabilities. Together, these defects determine the TL glow-curve structure and dose response (Menon et al., 2015; Mohapatra et al., 2023; Stagi et al., 2024; Xiang et al., 2026).

For dosimetric use, preheating (thermal cleaning) is a standard protocol to selectively empty shallow traps and isolate a stable main dosimetric peak, improving reproducibility and minimizing low-temperature spurious signals (Kortov, 2007; Kron and Lonski, 2021; Parisi et al., 2020; Polymeris et al., 2021). Studies on rare-earth-doped borate phosphors and borate glasses show that appropriate preheating can suppress low-temperature peaks while preserving deeper traps responsible for high-temperature dosimetric maxima. Dose–response investigations typically reveal linear behavior over broad dose ranges before transitioning to sublinear or saturating regimes as traps progressively fill, with many borate hosts exhibiting favorable linearity, low fading, and good reusability (Anishia et al., 2011; Chen et al., 1981, 1996). These characteristics are essential for reliable dosimetry, particularly in applications requiring stability and repeatability.

The influence of heating rate on TL glow curves provides a sensitive probe of recombination mechanisms and trap interactions. In the "classical" regime, increasing heating rate shifts TL peaks to higher temperature while maintaining an approximately constant or gently varying integrated intensity, in line with conventional general-order kinetics (Bakr and Omer, 2020; Madkhali et al., 2025; Mammadov et al., 2024; Sarkar et al., 2024; Yüksel et al., 2018). However, a growing number of inorganic materials, including borate-based phosphors and single crystals, exhibit anomalous heating rate behavior, where TL intensity or peak area increases or decreases in a non-monotonic or unexpected manner with heating rate. Variable-heating-rate experiments have revealed anomalous behavior in several borate hosts, including $YAl_3(BO_3)_4$:Sm^{3+}, $Ca_4LaO(BO_3)_3$, $La_2CaB_{10}O_{19}$:Dy^{3+}, and Sm^{3+}-doped $YCa_4O(BO_3)_3$. These observations deviate from standard kinetic expectations. More advanced descriptions, including semi-localized transition models and inverse thermal-quenching concepts, are therefore often required (Chen and Pagonis, 2017; Delice et al., 2014; Madkhali et al., 2023). Such deviations indicate that simple first- or general-order kinetic assumptions are often insufficient to describe TL processes in complex borate systems. Theoretical studies have shown that several mechanisms can modify the conventional heating-rate dependence. These mechanisms include competition between recombination channels, the presence of charge reservoirs, and the simultaneous thermal release of electrons and holes. Their combined effects may lead to anomalous TL behavior. (Chen and Pagonis, 2017).

To disentangle these complex processes, advanced kinetic analysis tools have become indispensable. The variable heating rate (VHR) method tracks the shift of glow peak maxima with heating rate to extract activation energy and frequency factor; however, its reliability may deteriorate in the presence of anomalous heating-rate effects, strong retrapping, or thermal quenching. The various–heating-rate (VHR) method tracks the shift of glow-peak maxima with heating rate to obtain effective activation energies and kinetic (attempt) orders under diverse kinetic models, including general-order and OTOR/NMTS frameworks, where it can yield accurate or even model-independent activation energies in "classical" cases (Chen et al., 2022; Rasheedy and Abd-Elmageed, 2007; Sarkar et al., 2024). However, the reliability of VHR deteriorates when additional effects perturb the simple peak-shift picture. Thermal quenching can cause systematic overestimation of activation energy and erroneous quenching parameters if uncorrected quenched peaks are used, requiring empirical correction formulas or modified expressions that explicitly include luminescence efficiency to reduce errors (Maghrabi et al., 2022). Temperature-lag artifacts likewise distort the apparent T_{max}–β relation and make activation energy appear to vary with heating rate, but applying lag corrections restores consistent trapping parameters across β and improves VHR fits (Alajlani et al., 2021; Delice, 2018).

Rare-earth-containing borate hosts offer an additional layer of complexity and opportunity. In many glassy and crystalline borate matrices doped with Dy^{3+}, Sm^{3+}, Tb^{3+}, Nd^{3+} or other lanthanides, host-related defects such as borate radicals, sulfate groups, and oxygen vacancies serve as traps, while RE^{3+} ions provide efficient luminescent centers for recombination (Annalakshmi et al., 2014; Mohapatra et al., 2023). Spectroscopic studies show that RE^{3+} ions can modify local structure, alter trap energetics. They may also participate in energy transfer and cross-relaxation processes. These effects influence both steady-state luminescence and thermally stimulated emission (Mohan et al., 2017; Pisarska et al., 2018). In crystalline borate hosts, rare-earth cations form an integral part of the lattice and may influence intrinsic defect formation. Their 4f levels can also serve as effective recombination centers. Consequently, intrinsic defect states may be coupled to rare-earth-related luminescent transitions. This dual structural and luminescent role distinguishes these systems from conventional doped phosphors, leading to non-classical TL behavior governed by the interplay between intrinsic traps, RE-centered recombination, and non-radiative processes (Khamaganova, 2023; Zhou et al., 2022).

Despite the extensive literature on rare-earth-doped borate phosphors and borate glasses, and on intrinsic TL in undoped borate hosts, systematic studies on TL in rare-earth-based borate lattices where the rare-earth ion is an integral part of the host framework rather than a dopant remain relatively scarce (Daniel et al., 2018; Halefoglu et al., 2020; Pisarska et al., 2018; Vimalathithan et al., 2025). This lack of studies is particularly evident in systems where structural and luminescent roles of rare-earth ions are inherently coupled. In such systems, exemplified by Sm-containing borate frameworks, the rare-earth cation not only provides luminescent 4f centers but also plays a structural role that can profoundly influence defect chemistry, trap distributions, and recombination dynamics. The intrinsic coupling of Sm^{3+} to the borate network can generate characteristic defect complexes and recombination channels distinct from those in conventionally doped materials. Consequently, these materials are expected to exhibit distinct TL behavior compared to conventional doped systems. Yet, the impact of this rare-earth-based host character on TL glow-curve structure, dose response, anomalous heating rate behavior, and detailed kinetic parameters has not been comprehensively clarified. In particular, the correlation between intrinsic defect structures and non-classical TL responses remains largely unresolved.

Although anomalous heating-rate effects have been reported in various TL materials, systematic studies combining VHR and T_m–T_{stop} analyses remain limited. Consequently, the underlying charge-carrier dynamics and recombination mechanisms are not yet fully understood. (Alajlani et al., 2023a; Sonsuz et al., 2022). The interplay between trap distributions, recombination center topology, and charge-carrier competition under varying thermal protocols remains a key open issue for both fundamental TL theory and the optimization of dosimetric performance.

In this context, the present work focuses on the TL properties of a borate-based phosphor with $SmBa_3B_9O_{18}$ host lattice, in which Sm^{3+} is an integral constituent of the crystal framework rather than an external

dopant. In this rare-earth-based host, Sm^{3+} is expected to contribute directly to the formation of intrinsic defect complexes and to act as a principal recombination center for thermally released carriers, thereby strongly coupling structural defects and luminescent output. This intrinsic coupling provides a unique platform for investigating non-classical TL behavior in complex borate systems. This study employs preheating protocols, dose–response measurements, and systematic heating-rate experiments. Advanced kinetic analyses, including VHR, T_m–T_{stop}, and multi-peak glow-curve deconvolution, are also applied. These approaches are used to investigate the relationships among intrinsic defects, trap distributions, and glow-curve characteristics in $SmBa_3B_9O_{18}$. Particular emphasis is placed on interpreting anomalous heating-rate behavior in relation to defect states, carrier dynamics, and competing recombination pathways. Clarifying these mechanisms in a rare-earth-based borate host is expected to advance the understanding of anomalous TL kinetics and to assess the potential of $SmBa_3B_9O_{18}$ for accurate and reliable dosimetric and luminescent applications.

2. Experiments

2.1. Material synthesis

$SmBa_3B_9O_{18}$ nanostructures were synthesized via a sol–gel assisted microwave combustion method. High-purity Sm_2O_3, $Ba(NO_3)_2$, and H_3BO_3 were used as precursor materials, while urea and glycine served as mixed fuels. All reagents were weighed according to stoichiometric ratios.

Initially, Sm_2O_3 was dissolved in 1 N HNO_3 under controlled heating. Subsequently, $Ba(NO_3)_2$ and H_3BO_3 were added, and the solution was diluted with deionized water to obtain a homogeneous mixture. After the addition of urea and glycine, the solution was stirred at 80 °C for 1 h to form a stable sol. Continuous heating led to gel formation via solvent evaporation.

The obtained gel was subjected to microwave-assisted combustion, producing a voluminous porous precursor due to rapid gas evolution. The overall combustion process can be described by an idealized redox reaction between metal nitrates (oxidizers) and organic fuels (urea and glycine), yielding the target phase along with gaseous by-products such as CO_2, N_2, and H_2O:

$$Sm_2O_3 + 3Ba(NO_3)_2 + 18H_3BO_3 + fuel \rightarrow 2SmBa_3B_9O_{18} + CO_2 + N_2 + H_2O \quad (1)$$

It should be noted that this equation represents an idealized reaction pathway, while the actual combustion involves complex intermediate steps and transient species.

The as-combusted powders were calcined at 800 °C for 4 h in air to remove residual organics and enhance crystallinity. The resulting $SmBa_3B_9O_{18}$ nanostructures were stored in a desiccator prior to further characterization.

2.2. Structural (XRD) and thermoluminescence characterization

Structural characterization was performed by powder X-ray diffraction (XRD) using a Malvern Panalytical Empyrean diffractometer operating in Bragg–Brentano geometry. The diffraction data of the synthesized $SmBa_3B_9O_{18}$ sample were collected over a 2θ range of 10°–80° with a step size of 0.02°, ensuring sufficient angular resolution for reliable phase identification and peak analysis. The instrument was operated at 45 kV and 40 mA, providing high-intensity Cu Kα radiation. The acquisition conditions were optimized to achieve good counting statistics and accurate determination of crystallographic features.

TL measurements were carried out using a Lexsyg Smart TL/OSL reader (Freiberg Instruments, Germany) (Richter et al., 2015) located at Bakırçay University. The system is equipped with a built-in $^{90}Sr/^{90}Y$ β irradiation source, delivering a nominal dose rate of 1.436 Gy s^{-1}. Prior to TL readout, samples were irradiated at room temperature with controlled β doses. TL glow curves were recorded under computer-controlled linear heating conditions, ensuring precise regulation of heating rate and temperature stability. Appropriate optical filters were employed to selectively detect the relevant emission bands, as discussed in the sections on filter-dependent measurements and kinetic analysis. The automated control of irradiation, heating, and detection parameters ensured high reproducibility and low experimental uncertainty across all TL measurements.

3. Results and discussions

3.1. Structural characterization and rietveld refinement analysis

The experimental XRD pattern in Fig. 1a matches well with the standard reference pattern (JCPDS card No. 061-0392), with all observed diffraction peaks indexed to the $SmBa_3B_9O_{18}$ phase and no extra reflections attributable to secondary or impurity phases. This confirms that the combustion route yields a single-phase product with good crystallographic consistency over the entire 2θ range.

To obtain more detailed structural information, a full-pattern Rietveld refinement was performed on the XRD data, as shown in Fig. 1b. The refined pattern reproduces the experimental intensities and positions very closely, and the difference curve ($I_{obs} - I_{cal}$) remains small and featureless across all angles, indicating an excellent quality of fit. The Bragg reflection markers coincide with the main diffraction maxima, confirming that the adopted structural model correctly describes the crystal lattice of $SmBa_3B_9O_{18}$.

The refined unit cell parameters and reliability factors are summarized in the inset of Fig. 1b. The lattice parameters were determined as $a = 7.197$ Å, $b = 7.197$ Å, and $c = 17.442$ Å, with corresponding unit cell volume of 782.44 $Å^3$. The reliability factors obtained from the refinement were $\chi^2 = 2.33$, $R_p = 0.061$, $R_{wp} = 0.089$, and $R_{exp} = 0.032$, indicating a good agreement between the observed and calculated patterns.

The successful refinement demonstrates that the synthesized phosphor crystallizes in the expected $SmBa_3B_9O_{18}$ structure with well-defined long-range order. The good agreement between observed and calculated profiles, together with the absence of unindexed peaks, verifies both the phase purity and the reliability of the crystallographic parameters used in subsequent analysis.

The relatively low R-factors and acceptable χ^2 value further confirm the robustness of the refinement and the high crystallinity of the synthesized sample.

To gain further insight into the crystallographic characteristics of $SmBa_3B_9O_{18}$, the average crystallite size and lattice microstrain were evaluated using both the Debye–Scherrer and Williamson–Hall (W–H) methods. The Debye–Scherrer equation yielded an average crystallite size of approximately 70.11 nm, indicating the formation of well-crystallized particles.

The Williamson–Hall approach was further employed to separate the contributions of crystallite size and lattice strain to the peak broadening. The corresponding Williamson–Hall plot is presented in Fig. 1c. According to the Uniform Deformation Model (UDM), the relationship between peak broadening, crystallite size, and microstrain can be expressed as:

$$\beta \cos\theta = \frac{k\lambda}{D} + 4\varepsilon \sin\theta \quad (2)$$

The linear fit of the W–H plot (βcosθ versus 4sinθ), shown in Fig. 1c, provided a crystallite size of 71.69 nm and a microstrain value of 2.242×10^{-3}. As summarized in Table 1, the crystallite size estimated using the Debye–Scherrer method was 70.11 nm, with a corresponding dislocation density (δ) of 0.203×10^{-3} nm^{-2}. The crystallite sizes obtained from both methods are in close agreement, confirming the reliability of the structural analysis. The slight difference between the two

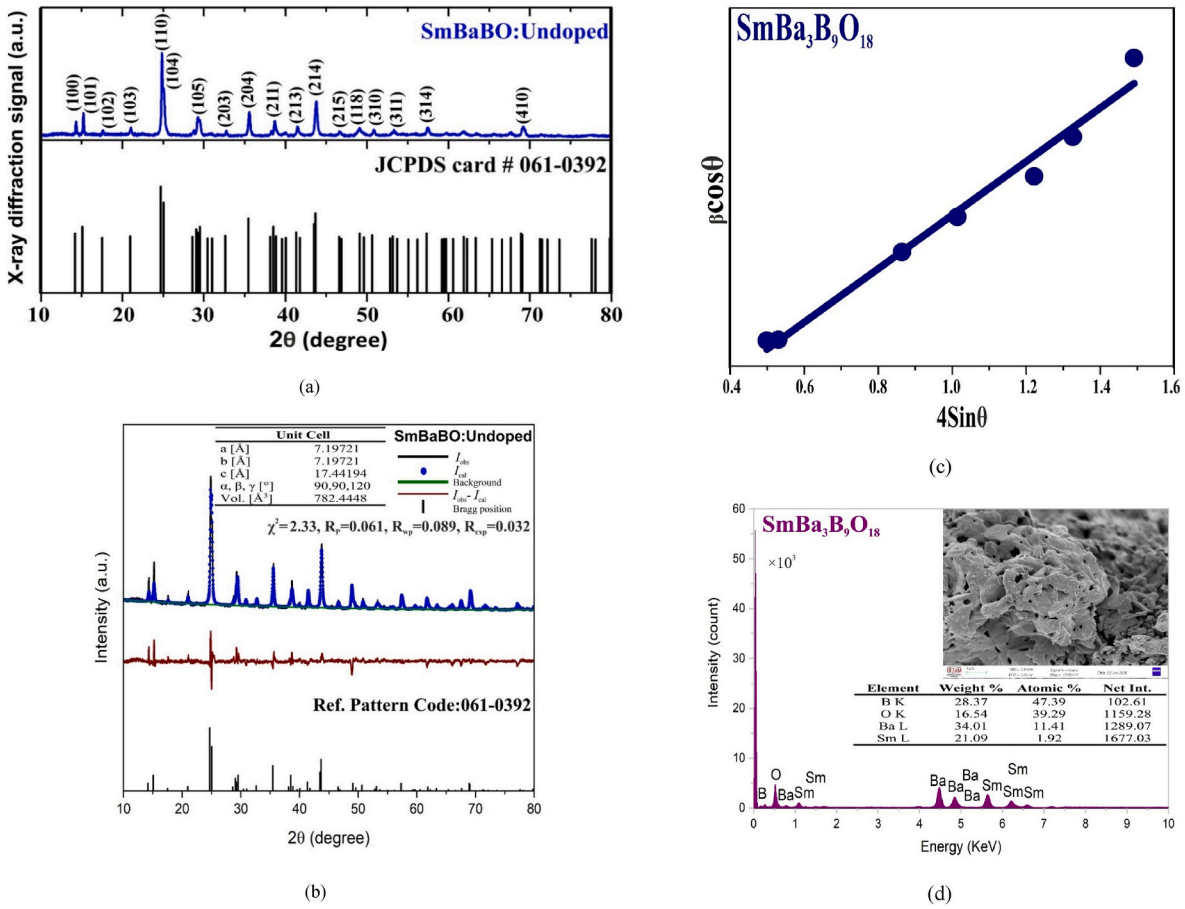

Fig. 1. Structural characterization of undoped SmBaBO phosphor: (a) X-ray diffraction (XRD) pattern of the synthesized sample along with the standard reference pattern (JCPDS card No. 061-0392), confirming phase purity and crystallographic consistency; (b) Rietveld refinement of the XRD data showing the observed (I_{obs}), calculated (I_{cal}), and difference ($I_{obs} - I_{cal}$) profiles, together with Bragg reflection positions (c) Williamson–Hall plot (βcosθ versus 4sinθ) of $SmBa_3B_9O_{18}$. (d) SEM micrograph and corresponding EDX spectrum of the synthesized $SmBa_3B_9O_{18}$ phosphor.

Table 1
Crystallite size (D), microstrain (ε), and dislocation density (δ) of $SmBa_3B_9O_{18}$ obtained from Debye–Scherrer and Williamson–Hall analyses.

Method		$SmBa_3B_9O_{18}$
Debye-Scherer	D (nm)	70.114
	$\delta \times 10^{-3}$ (nm^{-2})	0.203
Williamson-Hall	D (nm)	71.691
	$\varepsilon \times 10^{-3}$	2.242

values originates from the consideration of lattice strain effects in the Williamson–Hall model, which are neglected in the Scherrer approach. Furthermore, the relatively low microstrain value ($\varepsilon = 2.242 \times 10^{-3}$) indicates a minor degree of lattice distortion, while the low dislocation density ($\delta = 0.203 \times 10^{-3}$ nm^{-2}) suggests a reduced concentration of crystallographic defects within the $SmBa_3B_9O_{18}$ lattice. These findings demonstrate the good crystalline quality and structural homogeneity of the synthesized phosphor and are consistent with the excellent agreement observed in the Rietveld refinement results.

The morphology and elemental composition of the synthesized $SmBa_3B_9O_{18}$ phosphor were investigated using scanning electron microscopy (SEM) coupled with energy-dispersive X-ray spectroscopy (EDX), and the results are presented in Fig. 1d.

The SEM micrograph reveals highly agglomerated particles with a porous and irregular morphology. Such agglomeration is commonly observed in borate phosphors synthesized by combustion-assisted routes due to the rapid release of gaseous products during the combustion process. The observed aggregates are composed of interconnected nanocrystalline domains, which is consistent with the nanocrystalline nature inferred from the XRD analysis and the crystallite sizes (~70 nm) estimated using the Debye–Scherrer and Williamson–Hall methods.

The corresponding EDX spectrum confirms the presence of the constituent elements B, O, Ba, and Sm without any detectable impurity-related signals. Quantitative EDX analysis yielded elemental contents of 28.37 wt% B, 16.54 wt% O, 34.01 wt% Ba, and 21.09 wt% Sm. The observed elemental composition is in good agreement with the expected stoichiometry of $SmBa_3B_9O_{18}$, confirming the successful formation of the target phase.

The combined SEM and EDX results corroborate the structural findings obtained from XRD and Rietveld refinement, demonstrating the formation of chemically homogeneous $SmBa_3B_9O_{18}$ nanostructures with high phase purity. It should be noted that the crystallite size and microstrain values obtained from the Debye–Scherrer and Williamson–Hall methods are approximate estimates, since instrumental broadening and possible anisotropic strain effects were not explicitly considered.

3.2. Filter-dependent thermoluminescence glow curve analysis and selection of the 565 nm IRSL-TL signal

TL glow curves of the investigated sample were recorded using three different optical filter configurations centered at 365 nm (BSL), 410 nm (IRSL), and 565 nm (IRSL) following β irradiation with a dose of 50 Gy (Fig. 2). Such filter-controlled detection windows are widely used in

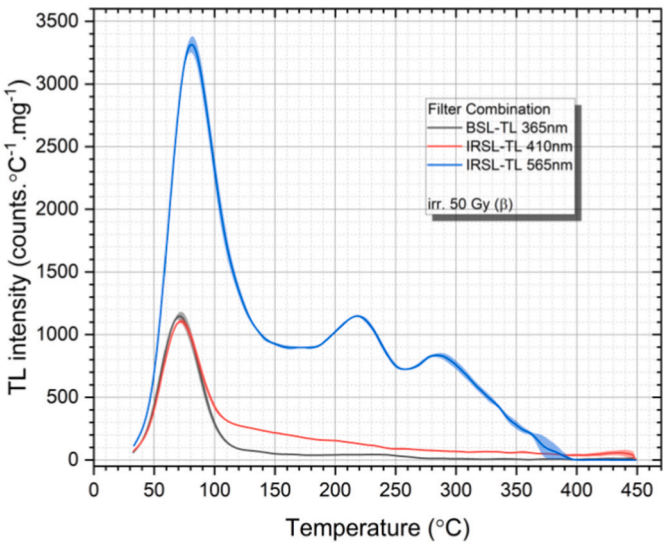

Fig. 2. TL glow curves of the investigated sample recorded after β irradiation with a dose of 50 Gy using different optical filters. The mean net signal from three measurements for each combination is shown, with the corresponding standard deviation values represented as deviation bands.

modern TL/OSL readers (e.g. BG3/BG39 "blue" windows and OG550/BG39 "yellow-green" windows) to isolate specific emission bands and suppress stimulation light (D et al., 2025; Gardenali Yukihara, 2023; Motta et al., 2023; Riedesel et al., 2023). The use of spectrally selective detection enables the differentiation of luminescence contributions and provides insight into the relationship between thermally stimulated trap release and wavelength-dependent emission components.

The obtained TL glow curves clearly exhibit a multi-peak structure, indicating the presence of several trapping levels with different thermal stabilities, consistent with typical multi-component TL behavior in phosphors and feldspars (Asfora et al., 2021; Barad et al., 2024; Pagonis et al., 2021). A prominent low-temperature peak is observed ~80 °C for all filter configurations, which can be attributed to shallow trapping centers. However, significant filter-dependent variation is observed beyond this region.

In particular, the IRSL-TL signal recorded using the 565 nm optical filter reveals additional well-defined peaks at higher temperatures. A second peak appears in the intermediate temperature range (~217 °C), followed by a third broader peak in the high-temperature region (~283 °C). These peaks are either weakly represented or nearly absent in the TL curves obtained using the 365 nm and 410 nm optical filters. This behavior suggests that the higher-temperature TL components, which are attributed to more thermally stable trapping centers, contribute more strongly to the signal detected within the 565 nm detection window.

Furthermore, the intensity of the TL signal strongly depends on the selected optical filter. The TL signal obtained using the 565 nm band-pass filter exhibits the highest overall intensity, especially in the intermediate- and high-temperature regions, indicating that emissions associated with these TL components are more strongly represented within this detection window. In contrast, the TL signal recorded using the 365 nm band-pass filter decreases rapidly after the main peak, indicating that it is mainly associated with shallow and less stable trapping centers. The 410 nm band—pass filter shows intermediate characteristics, with a distinct low-temperature peak but only limited sensitivity to the intermediate- and high-temperature TL components.

The observed filter-dependent variation in glow curve structure suggests the presence of multiple luminescence contributions and is consistent with a complex trapping–recombination system. The improved resolution of the intermediate- and high-temperature TL components in the signal obtained using the 565 nm band-pass filter is particularly advantageous for subsequent kinetic analysis and deconvolution.

Based on these findings, the IRSL-TL signal recorded using the 565 nm optical filter was selected for further analysis in this study. The higher signal intensity, combined with the clear separation of multiple glow peaks—especially in the intermediate and high-temperature regions—provides more suitable conditions for accurate determination of kinetic parameters such as activation energy and frequency factor. Consequently, all experimental and kinetic analyses presented in this study were performed using the TL data obtained with the 565 nm optical filter.

A definitive assignment of specific trapping centers or emission transitions to individual TL components would require complementary spectrally resolved and time-resolved luminescence measurements, which are beyond the scope of the present work.

3.3. *Effect of preheating on thermoluminescence glow curves and curve area analysis*

To investigate the thermal stability of trapping centers and to systematically evaluate the effect of thermal cleaning, preheating experiments were performed prior to TL readout. The TL glow curves were recorded without preheating and after preheating at selected temperatures, as presented in Fig. 3a. All measurements were carried out using the 565 nm optical filter.

The glow curve obtained without preheating exhibits a dominant low-temperature peak around 70–90 °C, followed by a complex structure extending into the intermediate and high-temperature regions, indicating the simultaneous contribution of shallow and deep trapping centers. With increasing preheating temperature, a progressive modification of the glow curve shape is observed, reflecting the gradual removal of thermally unstable (shallow) traps.

To quantitatively evaluate this behavior, the integrated TL intensity (curve area) was analyzed as a function of preheating temperature (T_{stop}), as shown in Fig. 3b. The curve area decreases monotonically with increasing T_{stop}, confirming the progressive depletion of trapped charge carriers. A noticeable change in slope is observed around 150 °C, which indicates a transition region where most shallow traps are effectively emptied. Beyond this temperature, the remaining TL signal is predominantly associated with deeper and more thermally stable trapping centers. This interpretation is consistent with the disappearance of the low-temperature peak in the corresponding glow curves.

Further insight into the thermal cleaning process was obtained by analyzing the variation of curve area as a function of preheating time at a fixed temperature (inset of Fig. 3b). The curve exhibits a rapid initial decrease followed by a gradual stabilization, indicating a two-stage detrapping process: a fast depletion of shallow traps and a slower response associated with deeper traps.

Although a plateau-like behavior is observed for both shorter (≈8 s) and longer (≈25 s) preheating durations, the optimal preheating time was selected as 8 s. This is because the essential removal of shallow traps is already achieved within this duration, while preserving the population and stability of deeper trapping centers. In contrast, longer preheating durations (e.g., 25 s) lead to a noticeable reduction in peak intensities, suggesting partial depletion or thermal redistribution of charge carriers from deeper traps. Such effects may distort the intrinsic glow peak structure and compromise the reliability of subsequent kinetic analysis. Therefore, 8 s was chosen as the optimal preheating duration, providing an effective balance between thermal cleaning and preservation of deeper trap characteristics.

Overall, the combined analysis of glow curve evolution and curve area reduction demonstrates that preheating is an effective method for isolating deeper trapping centers by removing shallow contributions. This approach minimizes peak overlap and ensures more reliable conditions for subsequent kinetic evaluations.

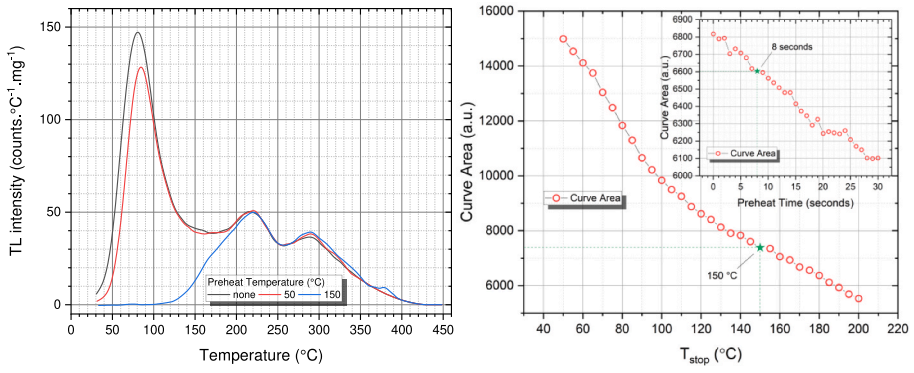

Fig. 3. (a) TL glow curves recorded with the 565 nm optical filter after different preheating conditions, showing the progressive removal of the low-temperature peak. (b) Curve area as a function of preheating temperature (T_{stop}), indicating gradual depletion of trapped charge carriers, with a transition around 150 °C. Inset: Curve area versus preheating time, showing rapid initial decay followed by a plateau; 8 s was selected as the optimal preheating duration.

3.4. Dose response and linearity analysis of TL glow curves

The dose-dependent TL response of the investigated sample was evaluated over a wide range of β irradiation doses, as presented in Fig. 4a. All measurements were carried out using the 565 nm optical filter and under identical experimental conditions. Fig. 4a shows the evolution of TL glow curves with increasing β dose. A systematic increase in TL intensity is observed across the entire temperature range, while the overall glow curve structure remains unchanged (Charak et al., 2021). Within experimental uncertainty, the positions of the two main glow peaks do not shift with increasing dose, indicating that the trapping and recombination mechanisms are preserved over the investigated dose range, and no significant peak shift or shape distortion occurs with increasing dose (Abishov et al., 2024; Espitia et al., 2022; Kalita and Chithambo, 2017). This invariance of T_{max} suggests that the effective trap depth and recombination scheme remain unchanged and is consistent with quasi first- or general-order kinetics, where peak shifts with dose are expected to be small in the absence of strong trap competition or restructuring (Cogollo et al., 2024; Horowitz et al., 2016). This indicates that the trapping and recombination mechanisms are preserved over the investigated dose range, and no significant peak shift or shape distortion occurs with increasing dose (Sena et al., 2025).

To quantify the dose response, the integrated TL intensity (curve area) was plotted as a function of β dose, as shown in Fig. 4b. The curve area exhibits a strong and nearly linear dependence on dose over a broad range. The data were fitted using a power-law function $y = a \cdot x^b$. For the total glow curve, the exponent b was found to be 1.02 in the 1.4–62 Gy range and 1.13 in the extended 1.4–500 Gy range, indicating a nearly linear response at low–intermediate doses and a tendency toward supralinearity at higher doses. A slight deviation from linearity at higher doses may be attributed to the onset of trap saturation or competition effects between trapping centers. Such supralinear trends at high doses are commonly associated with progressive filling of a hierarchy of traps and redistribution of carriers among competing trapping and recombination centers.

In addition to the total TL signal, the dose dependence of individual glow peaks was analyzed. Fig. 4c and d presents the variation of peak intensities (I_{m1} and I_{m2}) as a function of β dose for the intermediate and high-temperature peaks, respectively. For I_{m1}, the exponent b was determined as 1.03 in the 1.4–62 Gy interval and 1.19 in the 1.4–500 Gy range, while for Im2, the corresponding values are 1.01 and 1.29, respectively. These results confirm an almost linear response at lower doses and an increasingly supralinear behavior for both peaks at higher doses, following a similar trend as observed for the total curve area. The fact that both I_{m1} and I_{m2} exhibit comparable supralinear exponents in the high-dose regime suggests that the corresponding traps participate in a coupled trap–recombination network rather than acting as completely independent centers.

From a kinetic perspective, the combination of dose-independent peak positions and supralinear intensity growth suggests stable trap parameters with dose-dependent population effects. In such a scenario, the activation energy and attempt frequency remain essentially constant, while the effective kinetic order (governed by the balance between trapping, retrapping and recombination) gives rise to a non-linear filling behavior as dose increases. The absence of significant peak shifts indicates that the effective trap parameters remain relatively stable with dose. Together with the supralinear response of both main peaks, this observation suggests that progressive filling of a hierarchical trap system is likely to dominate at higher doses, although competition with deeper or non-radiative centers cannot be excluded.

Overall, the results demonstrate that the material exhibits a stable and reproducible TL response with good near linearity up to ~60 Gy and controlled supralinearity extending to 500 Gy, consistent with general-/mixed-order kinetic descriptions where supralinear dose response emerges from trap filling and competition with deeper or non-radiative centers (Bakr and Omer, 2020; Chen et al., 1996; Kitis and Pagonis, 2023; Nikiforov et al., 2017; Sunta et al., 2001). The absence of significant peak shifts and the near linear behavior of both the integrated signal and individual peak intensities at low–intermediate doses confirm the suitability of the material for dosimetric applications and are in line with reports of dose-independent T_{max} and quasi-first-order behavior in multi-trap systems. The extended supralinear range at higher doses may be advantageous for high dose dosimetry, provided that appropriate calibration curves and uncertainty analysis are implemented (Nemirovsky et al., 2023).

While the above results demonstrate a stable and nearly linear dose response over a wide range, it is also essential to evaluate the sensitivity of the material in the low-dose region, particularly in terms of its minimum detectable dose. The minimum detectable dose (MDD), also referred to as the lowest detectable dose limit (LDL), was determined to assess the sensitivity of the material at low radiation doses. The MDD was calculated using the relation (Pagonis and Kitis, 2006).

$$D_{LDL} = 3\sigma_{Bkg}\Phi_c \quad (3)$$

where σ_{Bkg} is the standard deviation of the background signal and Φ_c is the calibration factor defined as the ratio of the delivered dose to the corresponding net TL signal.

Based on this approach, the MDD value was found to be 128.893 ± 9.388 mGy. This result is consistent with the observed near-linear behavior in the low-dose region and confirms that the material is capable of reliably detecting sub-Gy dose levels. The relatively low MDD

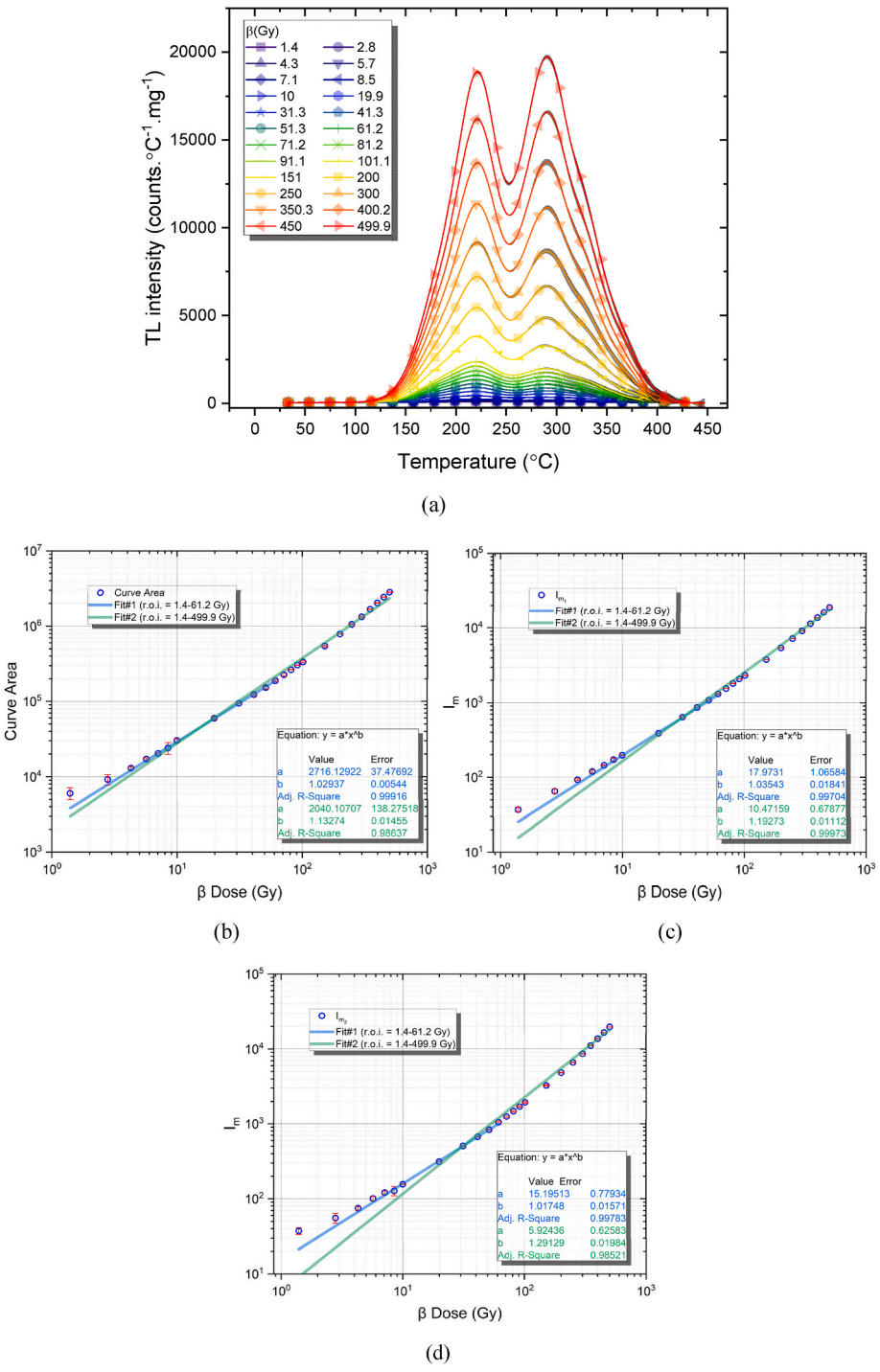

Fig. 4. (a) TL glow curves recorded at different β doses using the 565 nm optical filter, showing a systematic increase in intensity without significant change in peak shape. (b) Dose response of the integrated TL intensity (curve area) as a function of β dose, exhibiting near-linear behavior with slight supralinearity at higher doses. (c–d) Variation of peak intensities (I_{m1} and I_{m2}) with β dose for the intermediate and high-temperature peaks, respectively, both following a similar power-law dependence.

further supports the suitability of the material for practical dosimetric applications, particularly in situations where accurate low-dose measurements are required (Del Sol Fernández et al., 2016; Harvey et al., 2015; Panda et al., 2025).

3.5. Reusability of TL response

The reusability and repeatability of the TL response were evaluated through multiple consecutive irradiation–readout cycles under identical experimental conditions. The TL glow curves corresponding to successive readouts are presented in Fig. 5a. It is evident that the overall glow curve shape, peak positions, and relative intensities remain nearly unchanged over repeated measurements, indicating good stability of the trapping and recombination processes (Madkhali et al., 2025; Ullah et al., 2024).

To quantitatively assess the reproducibility of the TL signal, the integrated TL intensity (curve area) was analyzed as a function of readout order, as shown in Fig. 5b. The curve area values were normalized to the

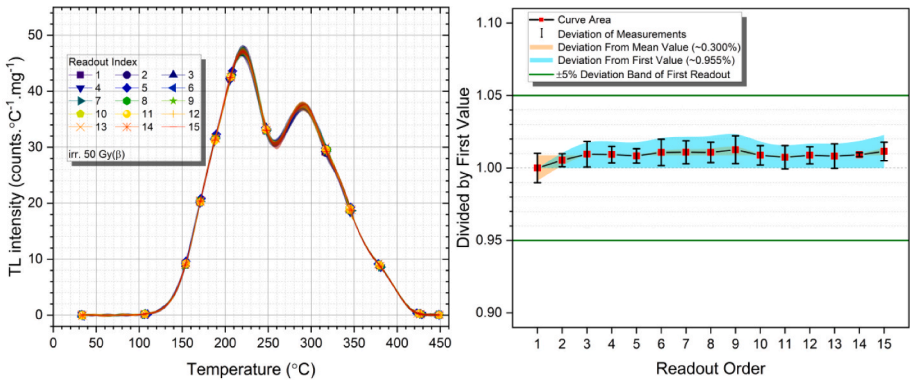

(a) (b)

Fig. 5. (a) TL glow curves recorded over multiple consecutive irradiation–readout cycles using the 565 nm optical filter, showing high reproducibility with no significant change in peak shape or position. (b) Normalized curve area as a function of readout order, demonstrating stable TL response with deviations within ±5%, confirming excellent reusability and repeatability of the material.

first measurement and plotted to evaluate deviations. The results show that the TL response remains highly stable, with fluctuations confined within a narrow range. The average deviation from the first readout was found to be less than 1%, while the deviation from the mean value is approximately 0.3%. Furthermore, all measurements fall well within the ±5% deviation band, which is generally accepted as a criterion for good reproducibility in TL dosimetric materials (Elsheikh et al., 2019; Muniz et al., 1995).

These results demonstrate that the material exhibits excellent reusability, with minimal signal degradation or sensitivity loss over repeated use. The stability of the TL response suggests that no significant alteration of trap structure or recombination efficiency occurs during repeated irradiation and readout cycles. This behavior confirms the suitability of the material for practical dosimetric applications where repeated measurements are required (Nattudurai et al., 2024).

3.6. Anomalous heating rate dependence of TL glow peak intensity

The effect of heating rate on the TL response of the investigated sample was examined in the range of 0.2–4 °C s^{-1} following β irradiation, as shown in Fig. 6a. As expected, increasing the heating rate results in a systematic shift of the glow peaks toward higher temperatures due to the reduced time available for thermal release of trapped charge carriers. Specifically, the first peak shifts from 187 °C to 230 °C, while the second peak shifts from 255 °C to 297 °C. However, in contrast to conventional TL behavior, a significant increase in peak intensity is observed with increasing heating rate.

The main glow peak intensity increases from approximately 36,000 to ~44,000 counts $°C^{-1}$ mg^{-1} as the heating rate increases from 0.2 to 4 °C s^{-1}. This change corresponds to an increase of approximately 22%. The normalized parameters presented in Fig. 6b support this observation. Both the integrated TL intensity and the individual peak intensities, I_{m1} and I_{m2}, increase systematically with heating rate. At the same time, the peak temperatures (T_{m1}, T_{m2}) shift monotonically to higher values, confirming the expected thermal activation behavior. The simultaneous increase in peak height and integrated TL intensity indicates anomalous heating-rate behavior rather than a simple redistribution of the glow-curve components.

This behavior clearly contradicts the predictions of the simple trap model (STM) and localized transition (LT) model, which assume heating-rate-independent TL output in the absence of thermal quenching and a decrease in intensity when quenching is present (Mandowski and Bos, 2011). The observed increase in both peak intensity and integrated TL signal therefore represents a typical example of anomalous heating-rate behavior (AHRB), also referred to as anti-quenching behavior (Hakami et al., 2022; Kaynar et al., 2023; Souadi et al., 2025).

A plausible interpretation of the observed behavior can be provided within the framework of the semi-localized transition (SLT) model. In this model, charge carriers remain partially correlated with nearby recombination centers and may undergo repeated trapping–detrapping cycles before recombination. Increasing the heating rate shifts the recombination process toward higher temperatures, where thermally

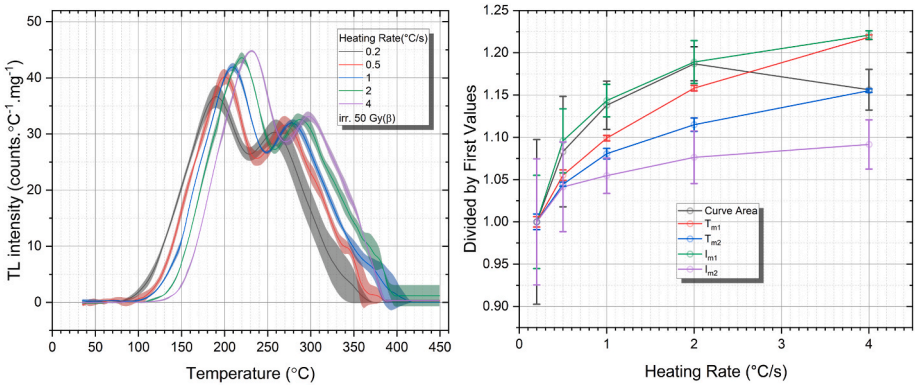

(a) (b)

Fig. 6. TL glow curves recorded at different heating rates (0.2–4 °C s^{-1}) following β irradiation (50 Gy). The glow peaks shift toward higher temperatures with increasing heating rate, accompanied by an increase in peak intensity (~22%), indicating anomalous heating rate dependence.

assisted delocalization may become more probable. Under strong retrapping conditions, this shift can modify the balance between retrapping, non-radiative losses, and radiative recombination (Mandowski, 2005).

The present results are consistent with this interpretation, particularly because the multi-peak glow curves indicate the presence of trapping levels with different thermal stabilities. At lower heating rates, the longer residence time within the relevant temperature range may increase the probability of retrapping and non-radiative loss, thereby reducing the TL intensity. At higher heating rates, the shorter residence time may limit these competing processes and favor recombination through luminescence centers, resulting in increased peak intensity and integrated TL output. More generally, this behavior is consistent with a complex multi-trap system in which heating rate alters the competition among trapping, retrapping, and recombination processes. Similar anomalous heating-rate effects have been attributed to strong retrapping and coupled trap–recombination dynamics in rare-earth-containing borates and related phosphors (Hakami et al., 2022; Yazan et al., 2021).

In addition, the role of thermal quenching (TQ) and thermal lag (TLA) must be considered. Thermal quenching generally reduces luminescence efficiency at elevated temperatures. However, its influence may be partially suppressed at higher heating rates because the sample remains at high temperatures for a shorter period. This can lead to an apparent anti-quenching effect, where the reduction of non-radiative losses contributes to an increase in observed TL intensity. Furthermore, thermal lag effects may shift the effective recombination temperature, indirectly influencing the balance between radiative and non-radiative processes.

The heating-rate-induced enhancement of both peak height and integrated TL intensity observed in this work is in good agreement with previous reports of anomalous heating-rate behavior (anti-quenching) in borate and related phosphors, where similar increases of high-temperature peaks with increasing heating rate were found in Sm^{3+}- and Dy^{3+}-activated $GdAl_3(BO_3)_4$, $YAl_3(BO_3)_4$, $Ca_4LaO(BO_3)_3$, ZnB_2O_4:Gd^{3+}, and LaB_3O_6:Ce^{3+} systems, as well as in intrinsic $K_7SrY_2(B_5O_{10})_3$ and other rare-earth-doped borates (Alajlani et al., 2023b; Alathlawi et al., 2025; Altowyan et al., 2023; Delice et al., 2019; Portakal Uçar, 2021). Similar heating-rate-dependent increases have been reported for several borate and rare-earth-containing phosphors and have been interpreted using SLT-based and other non-classical kinetic models (Mandowski and Bos, 2011; Pagonis et al., 2013).

Previous simulations and experiments have shown that non-classical recombination schemes can produce a heating-rate-dependent increase in the integrated TL signal, in contrast to the predictions of simple trap models (Chen and Pagonis, 2017; Maghrabi, 2018; Mammadov et al., 2024; Yüksel et al., 2018). The systematic changes in peak intensity, integrated TL signal, and peak temperature support a predominantly kinetic origin for the observed heating-rate dependence, although possible instrumental contributions are evaluated below. Similar behavior has been reported in materials such as YPO_4:Ce^{3+},Sm^{3+}, Eu^{3+}-doped borates, and Sm^{3+}-activated phosphors, where it has been successfully explained using SLT-based models and complex trap–recombination interaction mechanisms (Mandowski and Bos, 2011).

Overall, the anomalous increase in TL intensity with heating rate is consistent with several interacting processes. These may include semi-localized transitions, strong retrapping, trap competition, and heating-rate-dependent recombination efficiency. These findings indicate that conventional kinetic models alone may not adequately describe the observed TL behavior. The data are more consistent with a complex trap distribution involving coupled recombination pathways.

Despite the strong evidence supporting the intrinsic origin of the observed anomalous heating-rate behavior, it is also essential to consider possible experimental and thermal effects that may influence the apparent shift of peak temperatures. In particular, thermal lag (TLA), arising from temperature gradients between the sample and the heating element at higher heating rates, can lead to an overestimation of the measured peak temperature. Therefore, a correction procedure was applied to account for thermal lag effects and to obtain more accurate peak temperature values.

To correct for thermal lag effects, the following relation was employed:

$$T_j = T_i - \left(\frac{T_2 - T_1}{\ln\left(\frac{\beta_2}{\beta_1}\right)}\right) ln\left(\frac{\beta_i}{\beta_j}\right) \quad (4)$$

The variation of the uncorrected and corrected peak temperatures (T_{m1} and T_{m2}) with heating rate is shown in Fig. 7a and b. In both cases, peak temperatures increase with heating rate; however, the corrected data exhibit a reduced slope, indicating that part of the observed shift originates from thermal lag effects.

The magnitude of this correction increases with heating rate. For the first peak, ΔT_{m1} is negligible at low heating rates (0.2–0.5 °C s^{-1}), but increases to 0.35 ± 3.23 °C at 1 °C s^{-1}, 3.65 ± 3.72 °C at 2 °C s^{-1}, and 7.12 ± 5.22 °C at 4 °C s^{-1}. In contrast, the second peak shows smaller shifts, with ΔT_{m2} increasing from negligible values to 0.61 ± 2.30 °C, 0.75 ± 2.95 °C, and 2.45 ± 3.21 °C at 1, 2, and 4 °C/s, respectively.

The relatively small difference between corrected and uncorrected values indicates that thermal lag has a limited influence on the overall heating-rate dependence. Therefore, the observed behavior is mainly attributed to intrinsic kinetic processes rather than experimental artifacts.

3.7. Fading characteristics of TL glow peaks

The fading behavior of the TL signal was investigated over a time scale ranging from seconds to one day, as shown in Fig. 8a and b. Fig. 8a presents the evolution of the TL glow curves, while Fig. 8b shows the corresponding variation of the normalized logarithmic TL curve area. As seen in Fig. 8a, both glow peaks exhibit a noticeable increase in intensity during the initial storage period, reaching a maximum at approximately 12 h. This enhancement is particularly pronounced for both peaks, indicating that the TL signal does not follow a conventional monotonic fading behavior. Similar non-monotonic evolution of stored charge, involving an initial build-up followed by decay, has been reproduced in numerical TL/OSL models with competing trapping and fading processes and in systems where deep traps act as charge reservoirs influencing the active traps (Chen et al., 2015; Chen and Pagonis, 2020). After this maximum, a significant decrease in intensity is observed at longer storage times (1 day), suggesting the onset of dominant fading processes.

A clearer interpretation of this behavior is provided by the logarithmic representation in Fig. 8b. At short fading times, the TL signal remains nearly stable, showing only minor variations (<1%). However, after several hours, a systematic increase becomes evident, reaching a maximum of about 20.7% at 12 h. Beyond this point, the signal decreases sharply, returning nearly to the initial level after one day. Such time-dependent competition between filling and emptying of traps is consistent with simulations based on coupled rate equations, where the occupancy of the dosimetric trap increases up to a maximum and then relaxes toward an equilibrium value as excitation and thermal decay rates balance (Benavente et al., 2024; Chen et al., 2015).

The initial increase in TL intensity can be attributed to post-irradiation charge redistribution processes. Charge carriers trapped in shallow or metastable levels may migrate toward deeper and more stable traps over time, leading to an effective increase in the population of luminescent centers. ntertrap charge transfer from shallow to deeper, more stable traps has been inferred from TL dose-dependence and retrapping studies in oxides and nanostructured systems, where carriers are progressively accumulated in deeper levels due to strong retrapping and higher trapping cross sections (Debelo et al., 2016; Manju et al.,

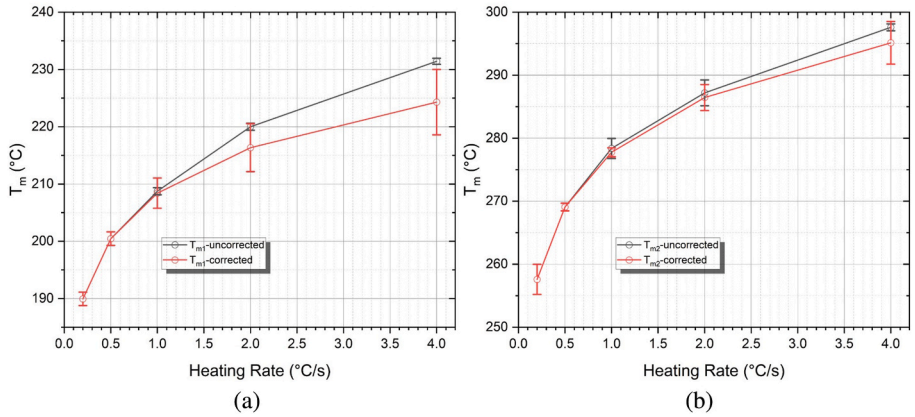

Fig. 7. Variation of the peak temperatures with heating rate before and after thermal lag correction: (a) first glow peak (T_{m1}) and (b) second glow peak (T_{m2}). Open symbols represent uncorrected data, while solid symbols correspond to thermally corrected values obtained using the logarithmic heating-rate relation.

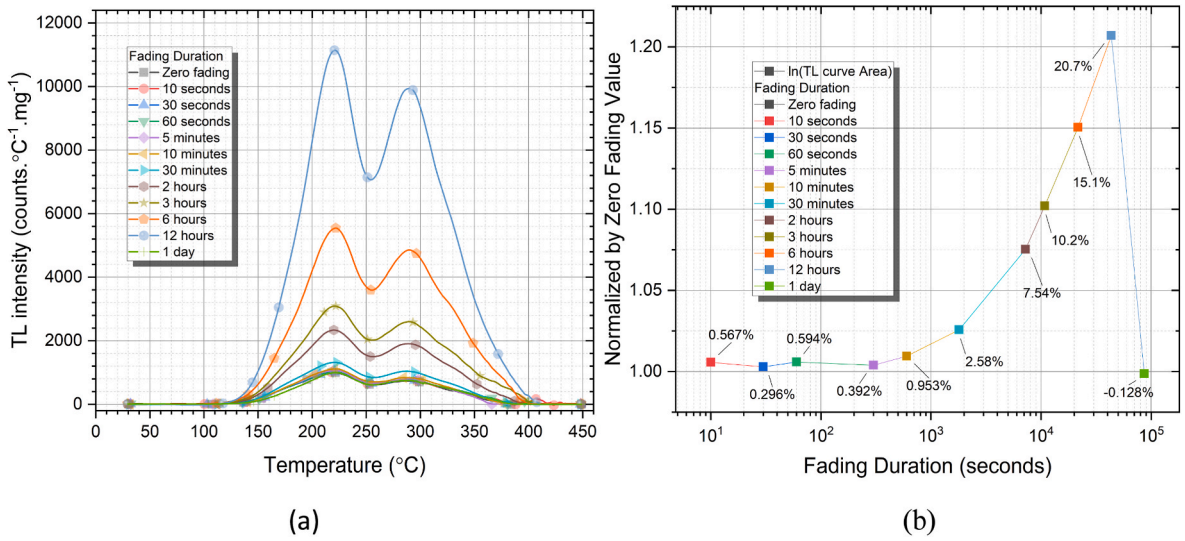

Fig. 8. Fading behavior of the TL signal over time: (a) evolution of TL glow curves at different fading durations, showing the variation in peak intensities; (b) normalized logarithmic TL curve area (ln(TL area)) as a function of fading time. The logarithmic representation highlights the non-monotonic trend, with an initial increase in intensity followed by a significant decrease after prolonged storage.

2020; Van der Heggen et al., 2020; Zhou et al., 2022). This thermally assisted retrapping process results in a temporary buildup of TL intensity. At longer fading times, the conventional fading mechanism dominates. The observed decrease after 12 h is associated with thermal release of trapped carriers and their subsequent non-radiative recombination, leading to a net loss of stored charge. Numerical simulations that include transitions between localized levels and non-radiative channels show that such thermally activated loss pathways are sufficient to reproduce significant TL fading and thermal quenching in dosimetric materials such as LiF:Mg,Ti (Benavente et al., 2024; Sorger et al., 2020).

Overall, the combined analysis of Fig. 8a and b indicates that the fading behavior is governed by a competition between charge redistribution (intensity enhancement) and thermal detrapping (signal loss). This non-monotonic trend further supports the presence of a complex trap structure with significant retrapping effects in the investigated material. This interpretation is in line with multi-trap/one-center and deep-trap-competitor models, where deep or thermally stable traps strongly modify the apparent fading kinetics of the main dosimetric peak and can mask simple exponential decay expected from single-trap parameters (Chen and Pagonis, 2017, 2020).

4. Kinetic parameters

4.1. Kinetic parameter evaluation using heating-rate methods with thermal lag correction

To evaluate the kinetic parameters of the two main dosimetric TL peaks (~220 and ~290 °C), a variable heating rate (VHR) approach was adopted. Two established methods were employed in this analysis: the Booth–Bohun–Parfianovitch (BBP) method (Bohun, 1954; Booth, 1954; Parfianovitch, 1954) and the Hoogenstraaten method (Hoogensraaten, 1958). TL glow curves were recorded over a range of heating rates between 0.2 and 4 °C s^{-1}, and the analysis was performed using both uncorrected and temperature lag-corrected peak temperatures in order to quantify the influence of instrumental effects on the evaluated trap parameters.

Within the Hoogenstraaten framework, the activation energy (E) was determined from the linear relationship between $\ln(T_m^2/\beta)$ and $1/(k_B T_m)$, where T_m denotes the peak temperature and β is the applied heating rate. As shown in Fig. 9, both corrected and uncorrected datasets exhibit strong linearity ($R^2 \approx 0.99$) for each glow peak, indicating that an effective single activation energy can describe the peak-shift behaviour over the investigated β range and that the peaks are kinetically well

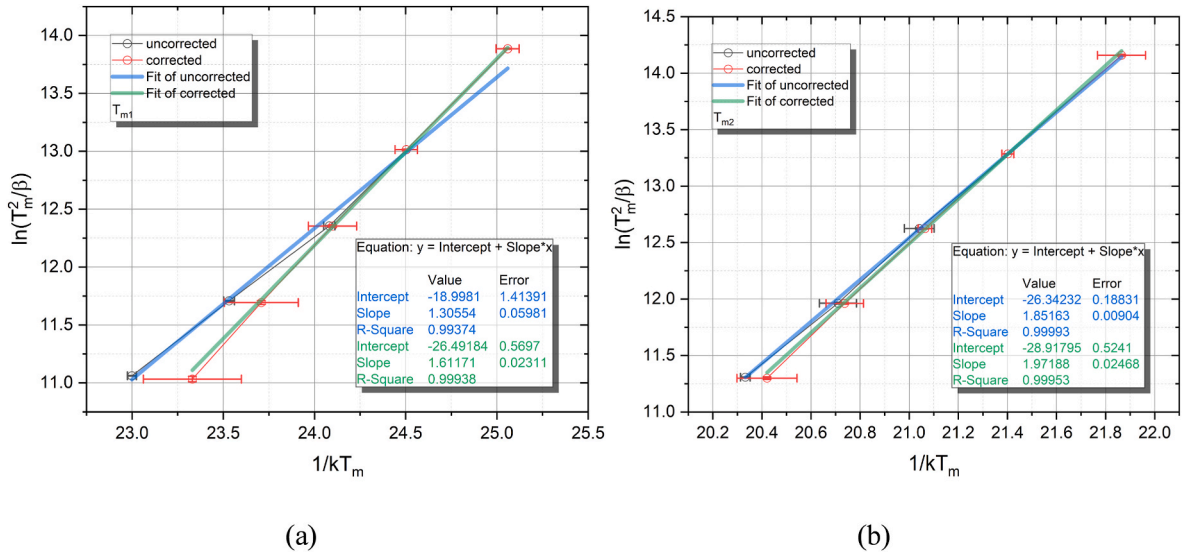

Fig. 9. Determination of activation energy (E_a) using heating-rate methods: (a) Hoogenstraaten plots of $\ln(T_m^2/\beta)$ versus $1/kT_m$ for the first glow peak (T_{m1}), and (b) corresponding plots for the second glow peak (T_{m2}).

separated. The activation energy was obtained from the slope of the fitted lines, while the frequency factor (s) was derived from the intercept.

In parallel, the BBP method was applied to calculate E using pairs of heating rates and their corresponding peak temperatures, according to:

$$E = k \cdot \frac{T_{m1} T_{m2}}{T_{m1} - T_{m2}} \cdot ln\left(\frac{\beta_1}{\beta_2} \cdot \left(\frac{T_{m2}}{T_{m1}}\right)^2\right) \quad (5)$$

where k is the Boltzmann constant, and T_{m1} and T_{m2} correspond to the peak temperatures measured at heating rates β_1 and β_2, respectively. In this study, T_{m1} refers to the value obtained at the lowest heating rate (0.2 °C s^{-1}), while T_{m2} corresponds to higher heating rates. For each peak, E values from all possible β-pairs in the 0.2–4 °C s^{-1} range were averaged to obtain representative effective activation energies.

As summarized in Table 2, both methods yield consistent activation energy values for the two glow peaks. For Maximum 1, the Hoogenstraaten method gives E_a values of 1.30 ± 0.06 eV (uncorrected) and 1.62 ± 0.02 eV (corrected), while the BBP method provides slightly higher values of 1.38 ± 0.21 eV and 1.70 ± 0.28 eV, respectively. Similarly, for Maximum 2, E_a increases from 1.85 ± 0.01 eV to 1.97 ± 0.02 eV (Hoogenstraaten) and from 1.89 ± 0.22 eV to 2.02 ± 0.30 eV (BBP) after applying thermal lag correction.

A systematic increase in activation energy is observed for both peaks upon applying thermal lag correction. This behavior indicates that the use of uncorrected peak temperatures leads to an underestimation of E_a, particularly at higher heating rates where thermal lag effects become more significant. This trend agrees with detailed analyses on ternary and quaternary crystals, where activation energies appeared to increase with heating rate when raw T_m values were used, but became mutually consistent and nearly β-independent once temperatures were corrected for the Kitis–Tuyn lag relation (Delice, 2018; Kitis and Tuyn, 1998).

Furthermore, the close agreement between the Hoogenstraaten and BBP results, especially after correction, supports the internal consistency of the VHR analysis. This convergence between two independent various-heating-rate formalisms is generally regarded as an indication of reliable kinetic parameter extraction in multi-trap systems and is consistent with comparative studies showing that different VHR variants (including Hoogenstraaten-type and two-rate methods) yield activation energies whose theoretical errors are smaller than typical experimental uncertainties and are largely independent of the kinetic order of the TL peak (Rasheedy and Abd-Elmageed, 2007; Singh et al., 1990).

4.2. T_m–T_{stop} experiment and initial rise (IR) method in $SmBa_3B_9O_{18}$

The TL trap structure was further investigated using the combined T_m–T_{stop} method and Initial Rise (IR) analysis, wo well-established approaches for analysing overlapping glow peaks and complex trap distributions in TL materials (Balci-Yegen et al., 2018; Pagonis et al., 2014). In the T_m–T_{stop} technique, the sample is preheated to a selected stop temperature (T_{stop}) prior to TL readout, allowing the progressive removal of charge carriers from shallow traps while preserving deeper ones. The evolution of the peak temperature (T_m) as a function of T_{stop} provides direct insight into the number and distribution of trapping levels.

The IR method, applied to the low-temperature side of each partially

Table 2
Calculated effective activation energies (E_a) for both TL glow peaks obtained using Hoogenstraaten and Booth–Bohun–Parfianovitch (BBP) methods. Results are presented for both uncorrected and thermal lag-corrected peak temperatures. BBP values represent averages over all possible heating-rate pairs in the range 0.2–4 °C s^{-1}.

Calculated Effective E_a (eV)					
β (°C s^{-1})	*Temp. Lag Effect Status*				*Method*
	Maximum 1		Maximum 2		
	Uncorrected	Corrected	Uncorrected	Corrected	
Average of Pairs of 0.2 to 4	1.38 ± 0.21	1.70 ± 0.28	1.89 ± 0.22	2.02 ± 0.30	Booth-Bohun-Parfianovitch Method
0.2 to 4	1.30 ± 0.06	1.62 ± 0.02	1.85 ± 0.01	1.97 ± 0.02	Hoogenstraaten's Method

cleaned glow curve, is based on the exponential dependence of TL intensity on temperature and allows the estimation of activation energy (E_a) without requiring assumptions about kinetic order (Coleman and Yukihara, 2018; Kitis et al., 2017; Van den Eeckhout et al., 2013). This approach is particularly effective for isolating individual trap contributions in materials exhibiting overlapping peaks and complex recombination pathways, although its accuracy can be affected by competition effects, peak overlap, retrapping and thermal quenching (Kitis et al., 2022).

In the present study, stepwise T_{stop} preheating experiments were performed over a wide temperature range, and the resulting TL glow curves are shown in Fig. 10a. As T_{stop} increases, the low-temperature components are progressively suppressed, while higher-temperature peaks become more pronounced. This behavior clearly indicates the presence of multiple trapping levels and significant peak overlap, consistent with TL systems exhibiting distributed trap energies similar to those reported for borate and related phosphors (Alathlawi et al., 2025; Pagonis et al., 2014; Souadi et al., 2023).

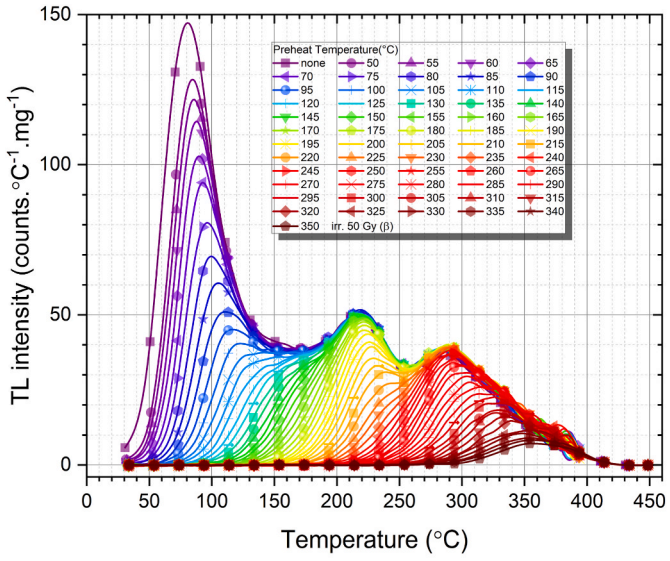

(a)

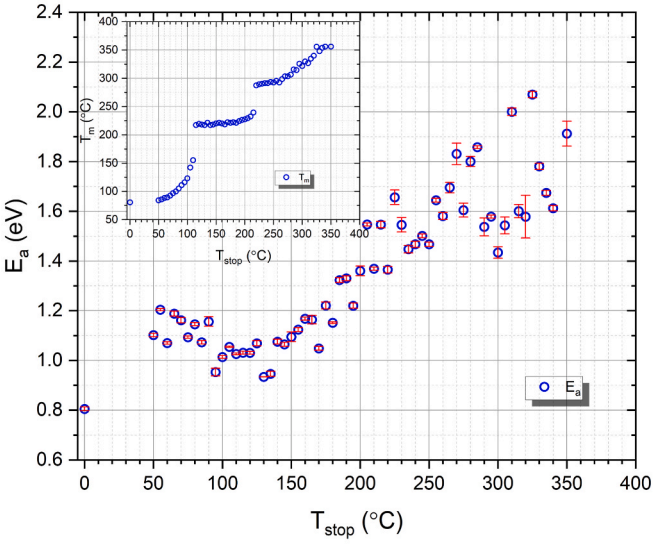

(b)

Fig. 10. TL analysis using the T_m–T_{stop} and Initial Rise (IR) methods: (a) TL glow curves recorded after stepwise preheating at different T_{stop} temperatures, illustrating the evolution of glow peak structure and intensity; (b) variation of activation energy (E_a) as a function of T_{stop} obtained using the Initial Rise method. The inset shows the corresponding T_m–T_{stop} plot, highlighting plateau and shifting regions associated with multiple trapping levels and possible trap distribution.

The corresponding T_m–T_{stop} p plot (Fig. 10b inset) reveals distinct plateau regions followed by systematic shifts of T_m toward higher temperatures. A near-linear increase of T_m at lower T_{stop} values, as observed here, has been reported in $Li_2B_4O_7$:Cu,Ag and other complex TL materials and is commonly interpreted as evidence for quasi-continuous or closely spaced overlapping traps rather than isolated, well-separated levels (Benavente et al., 2020; Bulcar et al., 2021; Sakurai and Gartia, 1997). However, it is important to emphasize that the T_m–T_{stop} analysis alone is not sufficient to unambiguously discriminate between discrete and continuous trap distributions. As demonstrated in earlier studies, reliable differentiation requires complementary techniques such as computerized glow curve deconvolution (CGCD/GCF) and detailed kinetic modelling (Benavente et al., 2019; Pagonis et al., 2014). Therefore, the present results should be interpreted as evidence of a complex and partially distributed trapping structure rather than a uniquely resolved trap configuration.

In contrast, the observed shifts in T_m at higher T_{stop} values indicate the depletion of these traps and the increasing contribution of deeper, more thermally stable trapping centers. Such plateau–shift behavior is widely recognized as evidence of either multiple discrete traps or a quasi-continuous trap distribution in TL materials.

Activation energies derived from the IR method exhibit a systematic increase with T_{stop}, as shown in Fig. 10b. This trend reflects the gradual transition from shallow to deeper trapping levels as preheating eliminates lower-energy traps. The continuous increase of E_a with T_{stop} suggests that the TL response is governed not by a single discrete trap, but by a distribution of trap depths contributing to the initial rise region. This behavior is consistent with previous studies where overlapping glow peaks and retrapping effects lead to T_{stop}-dependent effective activation energies.

Furthermore, the observed E_a values are in good agreement with those obtained from heating-rate methods (Hoogenstraaten and BBP), supporting the internal consistency of the kinetic analysis. This agreement indicates that both preheating-based (T_m–T_{stop}/IR) and heating-rate approaches probe the same effective trap structure, despite differences in experimental methodology.

Nevertheless, certain limitations should be considered. Due to significant peak overlap and the presence of retrapping, the strictly exponential region required for IR analysis may be restricted, and the extracted activation energies should therefore be interpreted as effective values rather than intrinsic single-trap parameters. Additionally, thermal redistribution and reduced signal intensity at higher T_{stop} values may introduce uncertainties in E_a estimation.

Overall, the combined T_m–T_{stop} and IR analysis demonstrates that the TL behavior of the studied phosphor is governed by a hierarchical trap system consisting of multiple overlapping and partially distributed trapping levels, consistent with the continuous or quasi-continuous energy distributions reported in feldspars, borate-based materials and other complex TL systems.

5. Conclusion

The present study demonstrates that $SmBa_3B_9O_{18}$, in which Sm^{3+} is an intrinsic constituent of the host lattice, combines structural robustness with a complex and non-classical TL response. X-ray diffraction and Rietveld refinement confirm the formation of a single-phase, well-ordered structure, providing a stable framework for defect formation and trap organization. Filter-dependent TL measurements and optimized preheating protocols reveal a clear hierarchy of trapping centers, where shallow traps can be effectively removed to isolate deeper, thermally

stable levels responsible for the intermediate- and high-temperature glow peaks. Dose–response analysis shows a nearly linear behavior up to ~60 Gy, followed by controlled supralinearity up to 500 Gy, together with a minimum detectable dose of 128.9 ± 9.4 mGy and excellent reproducibility over repeated irradiation–readout cycles, with an average deviation from the first measurement below 1% and all cycle-to-cycle variations remaining within ±5%.

A key outcome of this work is the clear manifestation of anomalous heating-rate behavior, where both peak intensities and integrated TL signals increase with heating rate. The main glow-peak intensity increases by approximately 22% when the heating rate is raised from 0.2 to 4 °C s^{-1}. This behavior deviates from conventional trap models and indicates the presence of semi-localized transitions, strong retrapping, and coupled trap–recombination dynamics. Complementary various-heating-rate, T_m–T_{stop}, and initial-rise analyses, including thermal-lag corrections, consistently reveal a hierarchical and partially distributed trap system, with effective activation energies of approximately 1.62–1.70 eV for the first main peak and 1.97–2.02 eV for the second main peak. In addition, the observed non-monotonic fading behavior, characterized by an initial increase in TL intensity followed by long-term decay, further supports the presence of charge redistribution and retrapping processes within a coupled trap system.

Overall, these results establish $SmBa_3B_9O_{18}$ as a promising rare-earth-based borate host for TL dosimetry, capable of reliable low- and high-dose measurements, while also providing a valuable model system for investigating non-classical TL kinetics, anomalous heating-rate effects, and complex trap–recombination mechanisms.

CRediT authorship contribution statement

Jabir Hakami: Formal analysis, Investigation, Methodology. **O. Madkhali:** Formal analysis, Investigation, Methodology. **M. Oglakci:** Investigation, Software. **E.A. Cin:** Investigation, Methodology. **E. Ekdal Karali:** Investigation, Methodology. **H. Orucu:** Investigation, Methodology. **M.B. Coban:** Methodology, Software. **U.H. Kaynar:** Investigation, Methodology. **N. Can:** Funding acquisition, Investigation, Methodology, Supervision, Writing – original draft, Writing – review & editing.

Declaration of competing interest

The authors declare that they have no known competing financial interests or personal relationships that could have appeared to influence the work reported in this paper.

Data availability

Data will be made available on request.

References

Abishov, A., Mammadov, S., Gurbanov, M., Ahadov, A., Ahadova, A., 2024. Thermoluminescence behavior and kinetic analysis of quartz under gamma irradiation. East Eur. J. Phys. 373–377. https://doi.org/10.26565/2312-4334-2024-4-43.

Alajlani, Y., Oglakci, M., Bulcar, K., Kaynar, Ü.H., Portakal-Uçar, Z.G., Alathlawi, H.J., Ayvacikli, M., Topaksu, M., Can, N., 2023a. Anomalous heating rate effect in GdAl3(BO3)4:Dy3+ under beta radiation stimulation: analysis of dose response and kinetic parameters. Ceram. Int. 49, 39967–39978. https://doi.org/10.1016/j.ceramint.2023.09.313.

Alajlani, Y., Oglakci, M., Kaynar, U.H., Ayvacikli, M., Portakal-Uçar, Z.G., Topaksu, M., Can, N., 2021. Thermoluminescence study and evaluation of trapping parameters of samarium doped barium silicate phosphor. J. Asian Ceram. Soc. 9, 291–303. https://doi.org/10.1080/21870764.2020.1864898.

Alajlani, Y., Sonsuz, M., Barad, A., Kaynar, Ü.H., Ayvacikli, M., Topaksu, M., Can, N., 2023b. Thermoluminescence in GdAl3(BO3)4 phosphors: unusual heating rate dependencies, dose responses and kinetic parameters. Appl. Radiat. Isot. 198, 110851. https://doi.org/10.1016/j.apradiso.2023.110851.

Alathlawi, H.J., Barad, A., Madkhali, O., Souadi, G., Sharahili, M., Hakami, J., Balci, S., Kaynar, U.H., Topaksu, M., Can, N., 2025. Intrinsic thermoluminescence and anomalous heating rate effects in undoped K7SrY2(B5O10)3 phosphors: a combined Tm–Tstop and GOK deconvolution study. Appl. Radiat. Isot. 225, 112092. https://doi.org/10.1016/j.apradiso.2025.112092.

Altowyan, A.S., Kaynar, Ü.H., Bulcar, K., Oglakci, M., Portakal-Uçar, Z.G., Hakami, J., Topaksu, M., Can, N., 2023. Unusual heating rates, dose responses and kinetic parameters detected on thermoluminescence from YAl3(BO3)4:Sm3+ phosphors. Ceram. Int. 49, 33291–33304. https://doi.org/10.1016/j.ceramint.2023.08.038.

Altowyan, A.S., Sonsuz, M., Kaynar, U.H., Hakami, J., Portakal-Uçar, Z.G., Ayvacikli, M., Topaksu, M., Can, N., 2024. Synthesis and thermoluminescence behavior of novel Sm3+ doped YCa4O(BO3)3 under beta irradiation. Ceram. Int. 50, 19681–19691. https://doi.org/10.1016/j.ceramint.2024.03.089.

Anishia, S.R., Jose, M.T., Annalakshmi, O., Ramasamy, V., 2011. Thermoluminescence properties of rare earth doped lithium magnesium borate phosphors. J. Lumin. 131, 2492–2498. https://doi.org/10.1016/j.jlumin.2011.06.019.

Annalakshmi, O., Jose, M.T., Madhusoodanan, U., Sridevi, J., Venkatraman, B., Amarendra, G., Mandal, A.B., 2014. Thermoluminescence mechanism in rare-earth-doped magnesium tetra borate phosphors. Radiat. Eff. Defect Solid 169, 636–645. https://doi.org/10.1080/10420150.2014.918128.

Asfora, V.K., Antonio, P.L., Gonçalves, J.A.C., Bueno, C.C., de Barros, V.S.M., Oliveira, C. N.P., Caldas, L.V.E., Khoury, H.J., 2021. Evaluation of TL and OSL responses of CaF2: Tm for electron beam processing dosimetry. Radiat. Meas. 140, 106512. https://doi.org/10.1016/j.radmeas.2020.106512.

Bakr, M., Omer, M., 2020. Determination of thermoluminescence kinetic parameters of La2O3 doped with Dy3+ and Eu3+. Materials 13, 1047. https://doi.org/10.3390/ma13051047.

Balci-Yegen, S., Boronat, C., Garcia-Guinea, J., Topaksu, M., Correcher, V., 2018. Correlation between thermoluminescence emission and phase transitions of tridymite. Phase Transitions 91, 1122–1128. https://doi.org/10.1080/01411594.2018.1515435.

Barad, A., Topaksu, M., Hakami, J., Can, N., 2024. Thermoluminescence kinetics in beta-irradiated novel ZnGa2O4:Eu3+ phosphor produced via gel combustion synthesis. Ceram. Int. 50, 11458–11468. https://doi.org/10.1016/j.ceramint.2024.01.046.

Benavente, J.F., Arquero, O., Berenguer-Antequera, J., 2024. Effects of trapped charge transitions between localized levels on the optical properties of thermoluminescent materials: a study of fading and thermal quenching. Opt. Mater. 156, 116006. https://doi.org/10.1016/j.optmat.2024.116006.

Benavente, J.F., Gómez-Ros, J.M., Correcher, V., 2020. Characterization of the thermoluminescence glow curve of Li2B4O7:Cu,Ag. Radiat. Meas. 137, 106427. https://doi.org/10.1016/j.radmeas.2020.106427.

Benavente, J.F., Gómez-Ros, J.M., Romero, A.M., 2019. Thermoluminescence glow curve deconvolution for discrete and continuous trap distributions. Appl. Radiat. Isot. 153, 108843. https://doi.org/10.1016/j.apradiso.2019.108843.

Bohun, A., 1954. Thermoemission und Photoemission von Natriumchlorid. Czech. J. Phys. 4, 91–93. https://doi.org/10.1007/BF01688114.

Booth, A.H., 1954. Calculation of electron trap depths from thermoluminescence maxima. Can. J. Chem. 32, 214–215. https://doi.org/10.1139/v54-027.

Bulcar, K., Cin, E.A., Hakami, J., Altowyan, A.S., Coban, M.B., Kaynar, U.H., Topaksu, M., Can, N., 2026. Dose-response and trap kinetics of Dy3+-doped LiCa4O(BO3)3 for thermoluminescence dosimetry. Mater. Sci. Semicond. Process. 210, 110679. https://doi.org/10.1016/j.mssp.2026.110679.

Bulcar, K., Oglakci, M., Kaynar, U.H., Ayvacikli, M., Souadi, G., Topaksu, M., Can, N., 2021. Thermoluminescence glow curve analysis and evaluation of trapping parameters of dysprosium doped lanthanum calcium borate La2CaB10O19. Nucl. Instrum. Methods Phys. Res. Sect. B Beam Interact. Mater. Atoms 489, 58–68. https://doi.org/10.1016/j.nimb.2020.12.023.

Charak, I., Manhas, M., Khajuria, P., Bedyal, A.K., Swart, H.C., Kumar, V., 2021. Investigation of thermoluminescence response and kinetic parameters of CaMgB2O5:Tb3+ phosphor against UV-C radiation for dosimetric application. J. Mater. Sci. Mater. Electron. 32, 17418–17426. https://doi.org/10.1007/s10854-021-06273-y.

Chen, R., Fogel, G., Lee, C.K., 1996. A new look at the models of the superlinear dose dependence of thermoluminescence. Radiat. Protect. Dosim. 65, 63–68. https://doi.org/10.1093/oxfordjournals.rpd.a031683.

Chen, R., Lawless, J.L., Pagonis, V., 2022. On the various-heating-rates method for evaluating the activation energies of thermoluminescence peaks. Radiat. Meas. 150, 106692. https://doi.org/10.1016/j.radmeas.2021.106692.

Chen, R., McKeever, S.W.S., Durrani, S.A., 1981. Solution of the kinetic equations governing trap filling. Consequences concerning dose dependence and dose-rate effects. Phys. Rev. B 24, 4931–4944. https://doi.org/10.1103/PhysRevB.24.4931.

Chen, R., Pagonis, V., Lawless, J.L., 2015. Time and dose-rate dependence of TL and OSL due to competition between excitation and fading. Radiat. Meas. 82, 115–121. https://doi.org/10.1016/j.radmeas.2015.09.006.

Chen, R., Pagonis, V., 2017. A model explaining the anomalous heating-rate effect in thermoluminescence as an inverse thermal quenching based on simultaneous thermal release of electrons and holes. Radiat. Meas. 106, 20–25. https://doi.org/10.1016/j.radmeas.2016.11.004.

Chen, R., Pagonis, V., 2020. A Monte-Carlo study of the fading of TL and OSL signals in the presence of deep-level competitors. Radiat. Meas. 132, 106257. https://doi.org/10.1016/j.radmeas.2020.106257.

Cogollo, R., Herrera, Jorge, Gutiérrez, O.D., 2024. Kinetic analysis and dosimetric characteristics of the thermoluminescent glow curve of aquamarine (Be3Al2(SiO3)6:Fe). Radiat. Phys. Chem. 221, 111748. https://doi.org/10.1016/j.radphyschem.2024.111748.

Coleman, A.C., Yukihara, E.G., 2018. On the validity and accuracy of the initial rise method investigated using realistically simulated thermoluminescence curves. Radiat. Meas. 117, 70–79. https://doi.org/10.1016/j.radmeas.2018.07.010.

D, R., A, R., T, K., R, P., K, D., 2025. Lexsyg luminescence measurement devices: status and outlook. Radiat. Meas. 181, 107377. https://doi.org/10.1016/j.radmeas.2025.107377.

Daniel, D.J., Panday, I.R., Kim, H.J., Kim, S., Fawad, U., 2018. Luminescence and low temperature trap centers in mixed rare earth borate crystal. J. Rare Earths 36, 1024–1029. https://doi.org/10.1016/j.jre.2018.02.011.

Debelo, N.G., Dejene, F.B., Mal'nev, V.N., Senbeta, T., Mesfin, B., Roro, K., 2016. Effect of retrapping on thermoluminescence peak intensities of small amorphous silicon quantum dots. Acta Phys. Pol., A 129, 362–366. https://doi.org/10.12693/APhysPolA.129.362.

Del Sol Fernández, S., García-Salcedo, R., Mendoza, J.G., Sánchez-Guzmán, D., Rodríguez, G.R., Gaona, E., Montalvo, T.R., 2016. Thermoluminescent characteristics of LiF:Mg, Cu, P and CaSO4:Dy for low dose measurement. Appl. Radiat. Isot. 111, 50–55. https://doi.org/10.1016/j.apradiso.2016.02.011.

Delice, S., 2018. Temperature lag effect on TL glow peaks: corrections on kinetic parameters. J. Lumin. 204, 81–88. https://doi.org/10.1016/j.jlumin.2018.07.044.

Delice, S., Bulur, E., Gasanly, N.M., 2014. Anomalous heating rate dependence of thermoluminescence in Tl2GaInS4 single crystals. J. Mater. Sci. 49, 8294–8300. https://doi.org/10.1007/s10853-014-8537-0.

Delice, S., Isik, M., Gasanly, N.M., 2019. Low temperature thermoluminescence of Gd2O3 nanoparticles using various heating rate and Tmax − Texc. Methods. Results Phys. 12, 1809–1813. https://doi.org/10.1016/j.rinp.2019.02.025.

Elsheikh, A., Abd El-Hafez, A., Ahmed, M., Abdul-Razek, Y., El-Nagdy, M., 2019. Quantification of various factors influencing repeatability and reproducibility of TLD-600 detector. Arab J. Nuclear Sci. Appl. 0–0. https://doi.org/10.21608/ajnsa.2019.13313.1219.

Espitia, Y., Cogollo, R., Osorio, A., Gutiérrez, O.D., 2022. Kinetic analysis of the main thermoluminescence glow peak in α-Al2O3. Radiat. Meas. 153, 106749. https://doi.org/10.1016/j.radmeas.2022.106749.

Gardenali Yukihara, E., 2023. TL and OSL as research tools in luminescence: possibilities and limitations. Ceram. Int. 49, 24356–24369. https://doi.org/10.1016/j.ceramint.2022.10.199.

Guler, I., Gasanly, N., 2018. Determination of trapping parameters of Tl 2 in 2 S 3 Se layered single crystal by thermoluminescence. Cryst. Res. Technol. 53. https://doi.org/10.1002/crat.201700134.

Hakami, J., Oglakci, M., Portakal-Uçar, Z.G., Sonsuz, M., Kaynar, U.H., Ayvacikli, M., Topaksu, M., Can, N., 2022. Samarium doped Ca3Y2B4O12 phosphor prepared by combustion method: anomalous heating rate effect, dosimetric features, and TL kinetic analyses. J. Lumin. 251, 119200. https://doi.org/10.1016/j.jlumin.2022.119200.

Halefoglu, Y.Z., Oglakci, M., Portakal, Z.G., Akca, S., Souadi, G.O., Canimoglu, A., Topaksu, M., Can, N., 2020. A study on thermoluminescence behaviour of Eu doped LaB3O6 irradiated with beta particles. Radiat. Phys. Chem. 168, 108571. https://doi.org/10.1016/j.radphyschem.2019.108571.

Harvey, J.A., Kearfott, K.J., Rafique, M., 2015. Dose response linearity and practical factors influencing minimum detectable dose for various thermoluminescent detector types. J. Radioanal. Nucl. Chem. 303, 1711–1718. https://doi.org/10.1007/s10967-014-3794-6.

Hoogensraaten, W., 1958. Electron traps in ZnS phosphorus. Philips Res. Rep. 13, 515–613.

Horowitz, Y.S., Eliyahu, I., Oster, L., 2016. Kinetic simulations of thermoluminescence dose response: long overdue confrontation with the effects of ionisation density. Radiat. Protect. Dosim. 172, 524–540. https://doi.org/10.1093/rpd/ncv495.

Joseph, T.A., Chopra, V., Dhoble, S.J., 2023. Thermoluminescence studies of zinc borate (ZnB 2 O 4) phosphor doped with rare earths for dosimetric aspects. Luminescence 38, 1597–1606. https://doi.org/10.1002/bio.4542.

Kalita, J.M., Chithambo, M.L., 2017. The influence of dose on the kinetic parameters and dosimetric features of the main thermoluminescence glow peak in α-Al2O3:C,Mg. Nucl. Instrum. Methods Phys. Res. Sect. B Beam Interact. Mater. Atoms 394, 12–19. https://doi.org/10.1016/j.nimb.2016.12.027.

Kaynar, Ü.H., Oglakci, M., Bulcar, K., Benourdja, S., Bakr, M., Ayvacikli, M., Canimoglu, A., Topaksu, M., Can, N., 2023. Comparison of thermoluminescence characteristics of undoped and europium doped YAl3(BO3)4 phosphor synthesized by combustion method: anomalous heating rate, dose response and kinetic analyses. Radiat. Phys. Chem. 204, 110657. https://doi.org/10.1016/j.radphyschem.2022.110657.

Khamaganova, T.N., 2023. Preparation, luminescence, and application of LiMeBO3 borates, me = Mg, Ca, Sr, Ba, Zn, Cd. Review. Kondensirovannye sredy i mezhfaznye granitsy = Condensed Matter and Interphases 25, 311–332. https://doi.org/10.17308/kcmf.2023.25/11256.

Kitis, G., Pagonis, V., Tzamarias, S.E., 2017. The influence of competition effects on the initial rise method during thermal stimulation of luminescence: a simulation study. Radiat. Meas. 100, 27–36. https://doi.org/10.1016/j.radmeas.2017.03.047.

Kitis, G., Sadek, A., Polymeris, G., Pagonis, V., 2022. Simulation of the effect of resolution between thermoluminescence peaks on the initial rise method of analysis. Nucl. Instrum. Methods Phys. Res. Sect. B Beam Interact. Mater. Atoms 524, 1–7. https://doi.org/10.1016/j.nimb.2022.05.004.

Kitis, G., Pagonis, V., 2023. Simulation of thermoluminescence signals at very low dose rates and low doses: implications for dosimetric applications. Radiat. Phys. Chem. 209, 110968. https://doi.org/10.1016/j.radphyschem.2023.110968.

Kitis, G., Tuyn, J.W.N., 1998. A simple method to correct for the temperature lag in TL glow-curve measurements. J. Phys. Appl. Phys. 31, 2065–2073. https://doi.org/10.1088/0022-3727/31/16/017.

Kortov, V., 2007. Materials for thermoluminescent dosimetry: current status and future trends. Radiat. Meas. 42, 576–581. https://doi.org/10.1016/j.radmeas.2007.02.067.

Kron, T., Lonski, P., 2021. Thermoluminescence dosimetry, in: radiation therapy dosimetry: a practical handbook. CRC press, names: Darafsheh, arash. In: Title: Radiation Therapy Dosimetry : a Practical Handbook/Edited by Arash Darafsheh. Description, first ed. CRC Press, Boca Raton, pp. 75–96. https://doi.org/10.1201/9781351005388-6. 2021.

Kumar, J., Yadav, A., Alvi, P.A., Kumar, S., Vij, A., 2019. Combustion synthesis and thermoluminescence response of near ultra-violet irradiated Mg2B2O5 nanophosphors. https://doi.org/10.1063/1.5097094.

Linderälv, C., Åberg, D., Erhart, P., 2021. Luminescence quenching via deep defect states: a recombination pathway via oxygen vacancies in Ce-Doped YAG. Chem. Mater. 33, 73–80. https://doi.org/10.1021/acs.chemmater.0c02449.

Madkhali, O., Bulcar, K., Barad, A., Zelai, T., Souadi, G., Alathlawi, H.J., Kaynar, U.H., Topaksu, M., Can, N., 2025. Thermoluminescence behaviour and kinetic analysis of a novel Tb^{3+}-Doped $LaCa_4O(BO_3)_3$ phosphor: impacts of heating rates and dose. Mater. Sci. Semicond. Process. 187, 109132. https://doi.org/10.1016/j.mssp.2024.109132.

Madkhali, O., Kaynar, Ü.H., Alajlani, Y., Coban, M.B., Guinea, J.G., Ayvacikli, M., Pierson, J.F., Can, N., 2023. Structural and temperature dependence luminescence characteristics of RE (RE=Eu3+, Dy3+, Sm3+ and Tb3+) in the new gadolinium aluminate borate phosphor. Ceram. Int. 49, 19982–19995. https://doi.org/10.1016/j.ceramint.2023.03.120.

Maghrabi, M., 2018. Dependence of the peak shift, peak height and FWHM of thermoluminescence peaks on the heating rate and trap parameters. J. Lumin. 198, 54–58. https://doi.org/10.1016/j.jlumin.2018.02.013.

Maghrabi, M., Al-Reyahi, A., Shaheen, A., Khattari, Z., Afaneh, F., 2022. Errors in the activation energy and thermal quenching parameters when evaluated from quenched thermoluminescence glow peaks using the various heating rates method. ECS J. Solid State Sci. Technol. 11, 046003. https://doi.org/10.1149/2162-8777/ac64c1.

Mammadov, S., Gurbanov, M., Ahadov, A., 2024. Exploring the thermoluminescent characteristics of nano α-Al2O3: influence of heating rate on glow peaks and activation energy. Eur. J. Chem. 15, 149–154. https://doi.org/10.5155/eurjchem.15.2.149-154.2552.

Mandowski, A., 2005. Semi-localized transitions model for thermoluminescence. J. Phys. Appl. Phys. 38, 17–21. https://doi.org/10.1088/0022-3727/38/1/004.

Mandowski, A., Bos, A.J.J., 2011. Explanation of anomalous heating rate dependence of thermoluminescence in YPO4:Ce3+,Sm3+ based on the semi-localized transition (SLT) model. Radiat. Meas. 46, 1376–1379. https://doi.org/10.1016/j.radmeas.2011.05.018.

Manju, Jain, M., Sen, D., Vij, A., Thakur, A., 2020. Estimating trap distribution and intertrap charge transfer in SrZnO2 nanoparticles. J. Phys. Chem. Solid. 136, 109052. https://doi.org/10.1016/j.jpcs.2019.05.049.

Menon, S.N., Kadam, S., Watanabe, S., Gundu Rao, T.K., Kulkarni, M.S., Babu, D.A.R., 2015. Thermoluminescence and defect centres in Tb doped lithium magnesium borate phosphor. J. Lumin. 167, 140–145. https://doi.org/10.1016/j.jlumin.2015.06.024.

Mohan, S., Kaur, S., Singh, D.P., Kaur, P., 2017. Structural and luminescence properties of samarium doped lead alumino borate glasses. Opt. Mater. 73, 223–233. https://doi.org/10.1016/j.optmat.2017.08.015.

Mohapatra, M., Suresh, A., Vinothkumar, P., Meena, G., Murugasen, P., 2023. Deciphering the role of gamma ray induced radicals in the thermoluminescence process of a neutral to cool daylight emitting Sr 1– x B 4 O 7 –Dy x phosphor through Electron Paramagnetic Resonance (EPR) spectroscopy. ACS Applied Optical Materials 1, 544–551. https://doi.org/10.1021/acsaom.2c00126.

Motta, S., Christensen, J.B., Frei, F., Peier, P., Yukihara, E.G., 2023. Investigation of TL and OSL detectors in ultra-high dose rate electron beams. Phys. Med. Biol. 68, 145007. https://doi.org/10.1088/1361-6560/acdfb2.

Muniz, J.L., Delgado, A., Ros, J.M.G., Brosed, A., 1995. Application of glow curve analysis methods to radiotherapy mailed dosimetry with LiF TLD-100. Phys. Med. Biol. 40, 253–268. https://doi.org/10.1088/0031-9155/40/2/004.

Nabadwip Singh, S., 2021. Analysis of the thermoluminescent of borate glass by computerized glow curve deconvolution in kinetic formalism. J. Phys., Conf. Ser. 2070, 012009. https://doi.org/10.1088/1742-6596/2070/1/012009.

Nattudurai, R., Sangeetha, L., Sivaraj, K., Kokila, P., 2024. New thermoluminescence dosimetric characteristics of Cu-doped Li2B4O7 phosphors with X-rays, gamma, and proton beams. J. Mater. Sci. Mater. Electron. 35, 2240. https://doi.org/10.1007/s10854-024-14015-z.

Nemirovsky, D., Oster, L., Reshes, G., Biderman, S., Bokobza, Y., Sterenberg, M., Eliyahu, I., Shapiro, A., Herman, B., Horowitz, Y., 2023. The thermoluminescence (TL) dose response of composite peak 5 in LIF:MG,TI (TLD-100): dependence on the order of kinetics. Radiat. Protect. Dosim. 199, 498–508. https://doi.org/10.1093/rpd/ncad032.

Ngoc, T., Ca, N.X., Ha, N.V., Thanh, L.D., Thuy, T.T.C., Du, P.T., Hung, N.M., Do, P. Van, 2024. Thermoluminescence properties of MSO4-B2O3 glasses doped with RE3+ (RE = Dy, Sm, Tb) ions and their applicability in radiation dosimetry. Opt. Mater. 149, 115088. https://doi.org/10.1016/j.optmat.2024.115088.

Nikiforov, S.V., Pagonis, V., Merezhnikov, A.S., 2017. Sublinear dose dependence of thermoluminescence as a result of competition between electron and hole trapping centers. Radiat. Meas. 105, 54–61. https://doi.org/10.1016/j.radmeas.2017.08.003.

Oglakci, M., Akça-Özalp, S., Portakal-Uçar, Z.G., Correcher, V., Benavente, J.F., Sonsuz, M., Can, N., Halefoglu, Y.Z., Topaksu, M., 2025. Thermoluminescence study of Nd3+ doped lanthanum tri-borate phosphor. J. Alloys Compd. 1013, 178570. https://doi.org/10.1016/j.jallcom.2025.178570.

Pagonis, V., Blohm, L., Brengle, M., Mayonado, G., Woglam, P., 2013. Anomalous heating rate effect in thermoluminescence intensity using a simplified semi-localized

transition (SLT) model. Radiat. Meas. 51–52, 40–47. https://doi.org/10.1016/j.radmeas.2013.01.025.
Pagonis, V., Brown, N.D., Peng, J., Kitis, G., Polymeris, G.S., 2021. On the deconvolution of promptly measured luminescence signals in feldspars. J. Lumin. 239, 118334. https://doi.org/10.1016/j.jlumin.2021.118334.
Pagonis, V., Morthekai, P., Kitis, G., 2014. Kinetic analysis of thermoluminescence glow curves in feldspar: evidence for a continuous distribution of energies. Geochronometria 41, 168–177. https://doi.org/10.2478/s13386-013-0148-z.
Pagonis, V., Kitis, G., 2006. Numerical and Practical Exercises in Thermoluminescence. Springer, New York, New York, NY. https://doi.org/10.1007/0-387-30090-2.
Panda, M., Chivukula, S., Joshi, S., Komathi, M.G., Annalakshmi, O., C, V.S., 2025. SMD chip resistors as reliable thermoluminescent dosimeters: dosimetric characterization and TL kinetics study. J. Lumin. 280, 121094. https://doi.org/10.1016/j.jlumin.2025.121094.
Parfianovitch, I.A., 1954. The determination of the depth of electron traps in crystal phosphors. J. Exp. Theor. Phys. 26, 696.
Parisi, A., Olko, P., Swakoń, J., Horwacik, T., Jabłoński, H., Malinowski, L., Nowak, T., Struelens, L., Vanhavere, F., 2020. Mitigation of the proton-induced low temperature anomaly of LiF:Mg,Cu,P detectors using a post-irradiation pre-readout thermal protocol. Radiat. Meas. 132, 106233. https://doi.org/10.1016/j.radmeas.2019.106233.
Pisarska, J., Kos, A., Sołtys, M., Górny, A., Pietrasik, E., Pisarski, W.A., 2018. Spectroscopy and energy transfer in Tb 3+/Sm 3+ co-doped lead borate glasses. J. Lumin. 195, 87–95. https://doi.org/10.1016/j.jlumin.2017.11.020.
Polymeris, G.S., Çoskun, S., Tsoutsoumanos, E., Konstantinidis, P., Aşlar, E., Şahiner, E., Meriç, N., Kitis, G., 2021. Dose response features of quenched and reconstructed, TL and deconvolved OSL signals in BeO. Results Phys. 25, 104222. https://doi.org/10.1016/j.rinp.2021.104222.
Portakal Uçar, Z.G., 2021. Thermoluminescence characteristics and kinetic analysis of beta irradiated Ca4LaO(BO3)3 phosphor. Cumhuriyet Sci. J. 42, 702–714. https://doi.org/10.17776/csj.929279.
Rasheedy, M.S., Abd-Elmageed, A.I., 2007. The validity of the two heating rates method to obtain the trapping parameters from general-order thermoluminescence glow peaks. J. Phys. Chem. Solid. 68, 243–248. https://doi.org/10.1016/j.jpcs.2006.11.002.
Richter, D., Richter, A., Dornich, K., 2015. Lexsyg smart - a luminescence detection system for dosimetry, material research and dating application. Geochronometria 42, 202–209. https://doi.org/10.1515/GEOCHR-2015-0022.
Riedesel, S., Duller, G.A.T., Ankjærgaard, C., 2023. Time-resolved infrared stimulated luminescence of the blue and yellow-green emissions – insights into charge recombination in chemically and structurally different alkali feldspars. J. Lumin. 257, 119724. https://doi.org/10.1016/j.jlumin.2023.119724.
Sakurai, T., Gartia, R.K., 1997. Evidence of continuous trap distribution in the glow curve of a Brown microcline. J. Appl. Phys. 82, 5722–5727. https://doi.org/10.1063/1.366436.
Sarkar, T.S., Sarkar, S., Bhattacharyya, S., Majumdar, P.S., 2024. A study toward the model Independence of various heating rates method in thermoluminescence glow curve analysis. Phys. Status Solidi 261. https://doi.org/10.1002/pssb.202400157.
Sena, P., Maya, H., Cogollo, R., 2025. Impact of dose and heating rate on thermoluminescence kinetics in aquamarine (Be3Al2(SiO3)6:Fe). Appl. Radiat. Isot. 216, 111593. https://doi.org/10.1016/j.apradiso.2024.111593.
Singh, T.S.C., Mazumdar, P.S., Gartia, R.K., 1990. A critical appraisal of methods of various heating rates for the determination of the activation energy of a thermoluminescence peak. J. Phys. Appl. Phys. 23, 562–566. https://doi.org/10.1088/0022-3727/23/5/014.
Sonsuz, M., Topaksu, M., Hakami, J., Can, N., 2022. Synthesis and thermoluminescence study of Eu doped novel LaBO3 phosphor: heating rate, dose response, trapping parameters. Radiat. Phys. Chem. 201, 110412. https://doi.org/10.1016/j.radphyschem.2022.110412.
Sorger, D., Stadtmann, H., Sprengel, W., 2020. Fading study and readout optimization for routinely use of LiF:Mg,Ti thermoluminescent detectors for personal dosimetry. Radiat. Meas. 135, 106342. https://doi.org/10.1016/j.radmeas.2020.106342.
Souadi, G., Bulcar, K., Akça-Özalp, S., Kaynar, U.H., Alathlawi, H.J., Madkhali, O., Sharahili, M., Somaily, D.A.E., Topaksu, M., Can, N., 2025. Anomalous heating rate dependence and kinetic analysis of Eu3+-activated K7SrY2(B5O10)3 borate phosphors. Ceram. Int. 51, 53432–53441. https://doi.org/10.1016/j.ceramint.2025.09.091.
Souadi, G., Kaynar, Ü.H., Sonsuz, M., Akça-Özalp, S., Ayvacikli, M., Topaksu, M., Ozmen, O.T., Can, N., 2023. Unravelling the impact of unusual heating rate, dose-response and trap parameters on the thermoluminescence of Sm3+ activated GdAl3(BO3)4 phosphors exposed to beta particle irradiation. Radiat. Phys. Chem. 213, 111211. https://doi.org/10.1016/j.radphyschem.2023.111211.
Stagi, L., Malfatti, L., Zollo, A., Livraghi, S., Carboni, D., Chiriu, D., Corpino, R., Ricci, P. C., Cappai, A., Carbonaro, C.M., Enzo, S., Khaleel, A., Adamson, A., Gervais, C., Falqui, A., Innocenzi, P., 2024. Phosphorescence by trapping defects in boric acid induced by thermal processing. Adv. Opt. Mater. 12. https://doi.org/10.1002/adom.202302682.
Sunta, C.M., Ayta, W.E.F., Chubaci, J.F.D., Watanabe, S., 2001. A critical look at the kinetic models of thermoluminescence: I. First-order kinetics. J. Phys. Appl. Phys. 34, 2690–2698. https://doi.org/10.1088/0022-3727/34/17/318.
Ullah, B., Kakakhel, M.B., Ur Rehman, S., Siddique, M.T., Munir, M., Ahmad, K., Mahmood, M.M., Wazir-ud-Din, M., Anjum, I., 2024. Synthesis and dosimetric characterization of lithium tetraborate (Li2B4O7:Cu,Ag) thermoluminescent dosimeter with improved reproducibility and reusability. Radiat. Phys. Chem. 220, 111704. https://doi.org/10.1016/j.radphyschem.2024.111704.
Van den Eeckhout, K., Bos, A.J.J., Poelman, D., Smet, P.F., 2013. Revealing trap depth distributions in persistent phosphors. Phys. Rev. B 87, 045126. https://doi.org/10.1103/PhysRevB.87.045126.
Van der Heggen, D., Vandenberghe, D., Moayed, N.K., De Grave, J., Smet, P.F., Joos, J.J., 2020. The almost hidden role of deep traps when measuring afterglow and thermoluminescence of persistent phosphors. J. Lumin. 226, 117496. https://doi.org/10.1016/j.jlumin.2020.117496.
Vimalathithan, R.M., Kumar, R.S., Suresh, G., Balaji, D., Balasaraswathy, S., Ponnusamy, V., 2025. Development of samarium and cerium doped yttrium orthoborate phosphor for near UV LED application. Asian J. Chem. 37, 2753–2758. https://doi.org/10.14233/ajchem.2025.34566.
Xiang, Y., Zhong, L., Long, Y., Liu, S., Cheng, Z., Rao, S., Hong, J., Lei, B., Suo, H., Zhang, J., Zhou, L., Wang, F., Wu, M., 2026. Deciphering defect-mediated anti-thermal quenching multimodal luminescence for information encryption. Adv. Mater. 38. https://doi.org/10.1002/adma.202515825.
Yazan, H., Portakal-Uçar, Z.G., Akça, S., Topaksu, M., Townsend, P.D., Can, N., 2021. Thermoluminescence of Ce and Nd co-doped CaF2 phosphors after beta irradiation. J. Lumin. 234, 117949. https://doi.org/10.1016/j.jlumin.2021.117949.
Yüksel, M., Dogan, T., Balci-Yegen, S., Akca, S., Portakal, Z.G., Kucuk, N., Topaksu, M., 2018. Heating rate properties and kinetic parameters of thermoluminescence glow curves of La-doped zinc borate. Radiat. Phys. Chem. 151, 149–155. https://doi.org/10.1016/j.radphyschem.2018.06.020.
Zhou, X., Ning, L., Qiao, J., Zhao, Y., Xiong, P., Xia, Z., 2022. Interplay of defect levels and rare earth emission centers in multimode luminescent phosphors. Nat. Commun. 13, 7589. https://doi.org/10.1038/s41467-022-35366-3.